Measurement of spatial coherence of light

JARI TURUNEN[1*], ATRI HALDER[1], MATIAS KOIVUROVA[2,3], AND TERO SETÄLÄ[1]

[1] Institute of Photonics, University of Eastern Finland, P.O. Box 111, FI-80101 Joensuu, Finland
[2] Tampere Institute for Advanced Study, Tampere University, FI-33100 Tampere, Finland
[3] Faculty of Engineering and Natural Sciences, Tampere University, FI-33720 Tampere, Finland
[*] Corresponding author: jari.turunen@uef.fi

Compiled November 18, 2022

The most frequently used experimental techniques for measuring the spatial coherence properties of classical light fields in space-frequency and space-time domains are reviewed and compared, with some attention to polarization effects. In addition to Young's classical two-pinhole experiment and several of its variations, we discuss methods that allow the determination of spatial coherence at higher data acquisition rates and also permit the characterization of lower-intensity light fields. These advantages are offered, in particular, by interferometric schemes that employ only beam splitters and reflective elements, and thereby also facilitate spatial coherence measurements of broadband fields.

http://dx.doi.org/10.1364/ao.XX.XXXXXX

1. INTRODUCTION

In their classic textbook *Principles of Optics* [1] Born and Wolf introduce the concept of spatial coherence of light with the aid of Young's two-pinhole interference experiment, and a similar introductory approach is used also by Mandel and Wolf in the book *Optical Coherence and Quantum Optics* [2]. Indeed, Young's experiment may be viewed as a definitive way to measure spatial coherence. Despite of its conceptual simplicity, Young's interferometer has certain inherent limitations, which have motivated the development of a wide range of alternative spatial coherence measurement techniques.

Perhaps the most obvious limitation of Young's two-pinhole setup is its low light efficiency, which makes the characterization of weak light fields difficult. Even though the selection of pinhole positions at the measurement plane is straightforward with modern spatial light modulators, the data acquisition time depends strongly on the required resolution and dimensionality of the problem. Another, more fundamental issue is related to coherence measurement of broadband light. In the standard textbooks [1, 2] spatial coherence is introduced by considering thermal light, which is converted to quasimonochromatic light by, e.g., a narrow-band spectral filter. If this is not done, and if the scale of the degree of spatial coherence depends on temporal frequency ω (as it usually does; see, e.g., Ref. [3]), Young's interference fringes become colored, which distorts the results of direct spatial coherence measurements.

In the present review, we revisit the motivation behind Young's interferometer and expand the discussion to more modern schemes. To limit the scope, we restrict the discussion to classical optical fields and second-order spatial coherence. Further, we discuss mainly coherence measurements in the paraxial domain (beam-like fields), where the coherence and polarization properties of light can be described in a unified way using 2×2 matrices [4]. We also concentrate on stationary fields, noting however that all of the techniques also apply to pulsed fields if the measurements are done, as usual, with 'slow' detectors that integrate over a single pulse or a section of a pulse train.

We begin with a qualitative discussion of Young's classic two-pinhole experiment in Sect. 2, providing intuitive arguments on the relationship between the fringe visibility and spatial coherence. In Sect. 3 we cover, again in qualitative terms, a selection of natural and man-made sources and fields with different states of coherence to motivate the need for development of diverse spatial coherence measurement techniques. Some experimental considerations, which are independent of the chosen technique, are also presented.

The sections to follow cover different techniques for coherence measurements, starting with a mathematical formulation of Young's interferometer in Sect. 4, along with its practical implementations and limitations. Most of the limitations can be alleviated by using wavefront folding or shearing interferometers, which form the subject of Sect. 5. In Sect. 6 we cover, though in less detail, a selection of other techniques for spatial coherence measurement. Certain subjects outside the main scope of the review are discussed in Sect. 7, before conclusions are drawn in Sect. 8.

2. INTERFERENCE IN YOUNG'S EXPERIMENT

Young's interferometer is of great historical value, and its original purpose was not the measurement of coherence at all; see Ref. [5] for a review of Young's experiment from all relevant perspectives. Instead of considering coherence, Thomas Young introduced the device to investigate the very nature of light. Already well before Young's time, this had been debated in length: did light consist of waves or corpuscles? In his landmark work *Opticks* [6], Newton laid out powerful arguments in favor of the corpuscular theory of light, overturning the wave theory described by Descartes [7]. This led to a long-standing consensus among scientists that light was indeed composed of minute particles.

It needs to be noted that in this era, natural sciences were almost entirely experimental, and the mathematical formalism did not exist as we know it today. The mathematical arguments were mainly geometrical in nature, while any relations to natural phenomena were philosophically motivated. In his now famous Bakerian Lecture published in 1802 [8], Young very carefully constructed arguments supporting the wave theory. After 32 pages of motivation, he finally brought forth the proposition: "Radiant Light consists in Undulations of the luminiferous Ether." In modern terms, he suspected light to consist of waves.

This was a radical proposition, contradicting the greatest natural philosopher ever. As is the case today, extraordinary claims require extraordinary proof. The first Bakerian Lecture gave a good motivation for this proposition, but it was by no means enough to convince the scientific community. Thus, Young designed, conducted, and analyzed several experiments in his second Bakerian Lecture published in 1804 [9], from which the first experiment later became known simply as the Young's experiment. He employed a thin card "about one-thirtieth of an inch in breadth," and placed it in the middle of a small hole pierced in thick paper, with light incident from the other side. Doing so, he observed interference fringes. Moreover, he noted that the presence of the card was required for the fringes to appear: "Now these fringes were the joint effects of the portions of light passing on each side of the slip of card, and inflected, or rather diffracted, into the shadow." This was interpreted as clear signature of wave behaviour, which Young illustrated in terms of spherical waves emerging from two pinholes (Fig. 1). He further constructed an analog model with water waves.

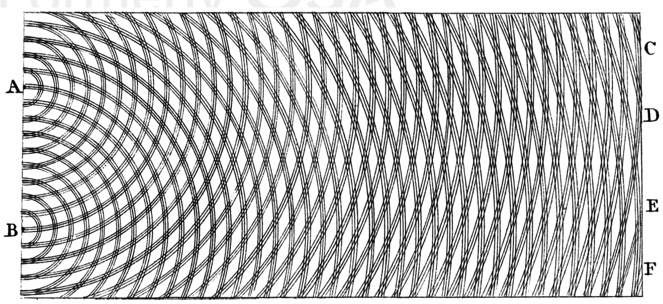

Fig. 1. Young's two-source interference diagram. Here sources A and B produce spherical waves, which yield minima at points C, D, E, and F in the observation plane. Reproduced from Ref. [10], page 777, Fig. 267.

Young's experiment formed the basis for further investigations on the wave nature of light, of which most notable studies were carried out by François Arago, Augustin-Jean Fresnel, Michael Faraday, and James Maxwell. These seminal investigations greatly advanced the mathematical explanation of the wave-optical point of view, and finally ascertained light as an electromagnetic phenomenon. However, the notion of coherence of light had not seriously entered the scientific discussion at this point yet, although some scattered ideas on the subject may already have existed.

The first significant investigations of spatial coherence were carried out in the mid 19th century by Émile Verdet [11], well after Young had passed away. But this did not ignite much interest, and research on coherence of light remained quite moderate. In the beginning of the 20th century, Max von Laue published the first measure of coherence of light [12], which was formulated largely in line with thermodynamics and employed the notion of entropy. Later, in 1934, Pieter van Cittert published an investigation on the joint probability distribution of light vibrations on a screen illuminated by an extended primary source [13]. Soon after, Fritz Zernike formulated the so called 'degree of coherence' [14], which is still one of the main theoretical tools used to quantify correlations today. With renewed interest, more researchers began to consider the coherence of light.

Soon after the second World War, there was great demand for an updated English textbook on optics. Until then, the textbook of choice was *Optik* by Max Born [15], but it was in German, and therefore many scientists showed interest towards an English translation of the book. As the field of optics had advanced greatly since the publication of *Optik*, Born determined that an entirely new book was required. In 1951, he hired Emil Wolf to work as his private assistant on preparation of the new book.

The project was extremely ambitious, with the idea of producing a textbook containing most of the relevant results in optics up to that time. In effect, the book would start from Maxwell's equations and move on to cover the areas of geometric optics, image formation, aberrations, interferometry, diffraction, acousto-optics, as well as optical properties of metals and crystals. This would truly form the *Principles of Optics*, as the name of the book suggests (although some subjects had to be excluded). According to accounts given by Wolf's students later on, compiling all of the relevant results into a single book took longer than expected, and Born got impatient. Born would have left the discussion on coherence out as he deemed it to be of minor interest, but Wolf insisted on including it. After additional publishing delays, the first edition finally came out in 1959.

Just a year later, in 1960, Theodore Maiman built the first functioning optical laser [16], which was largely based on the theoretical work of Charles Townes and Arthur Schawlow [17]. The theory relied heavily on the concepts of coherence of stationary sources, and thus, *Principles of Optics* became an instant landmark in optics research. To this day, it remains the all-time most-cited scientific work across all disciplines in physics.

During the time Wolf worked on the book, he was also publishing several of his findings. For example, he took the first steps in formulating a theory of interference and diffraction produced by realistic sources [18]. Moreover, he introduced the idea of partial coherence in concrete terms [19] and analyzed the intensity correlations found in the (then recent) experiments of Hanbury Brown and Twiss [20]. Further, Wolf showed for the first time that correlations in light also propagate as waves through free space [21], and derived the corresponding wave equations.

Notably, already at this stage Wolf had mathematically defined coherence as the ability of light to produce fringes in an interference experiment, although he did not explicitly state so. To illustrate this idea, Wolf drafted a "simple interference experiment" in Ref. [19], which was in fact a Young's interferometer. Wolf maintained this definition of coherence throughout the different editions of *Principles of Optics*, and explicitly stated in *Optical Coherence and Quantum Optics* that "The appearance of the fringes is said to be a manifestation of *spatial coherence* between the two light beams reaching [the point] P from the two pinholes P_1 and P_2..." (Ref. [2], page 151). It is largely thanks to Emil Wolf that Young's interferometer became one of the cornerstones of modern coherence research, although Thomas Young could not have foreseen such developments.

What Wolf considered in the context of Young's experiment was that the amplitude and phase may change at either pinhole. What we see in an experiment is then the time-averaged interference pattern, which is essentially an incoherent sum over the instantaneous patterns. This is qualitatively illustrated in Fig. 2; see also Visualization 1 for animations. To be more precise, when the amplitude of the field is decreased at one pinhole while remaining constant at the other, we see a decrease in visibility as shown in Fig. 2(a). On the other hand, if the amplitudes at the pinholes are equal (and constant) but one instead varies the relative phase between the pinholes, the interference pattern at the observation plane shifts as indicated in Fig. 2(b). Finally, if a field is partially coherent, the amplitudes at the two pinholes as well as the relative phase between them have random components. Thus, the instantaneous intensity at the observation plane has features from both Fig. 2(a) and Fig. 2(b), but it changes rapidly in time. Therefore, the time-averaged interference pattern looks like in Fig. 2(c), where the fringe visibility is reduced.

Since the difference in field amplitudes emerging from the two pinholes can be detected from the instantaneous visibility, and the phase difference from the position of the fringes, we can apply the same rationale to the time averaged interference pattern. However, due to the averaging, the interpretation changes slightly; instead of amplitude and phase differences we consider correlations between field fluctuations at the pinholes. The amplitude of the correlation function can then be determined from the visibility and its phase from lateral positions of the fringes, as we will describe in mathematical terms in Sect. 4.

3. PARTIALLY SPATIALLY COHERENT SOURCES AND FIELDS

We begin this section with a description of the basic concepts of coherence and propagation effects, including relationships between coherence at the source plane and the directionality of the radiated field, as well as the evolution of spatial coherence in free-space propagation. We then continue in Sect. 3B with a brief coverage of the spatial coherence and directionality properties of a selection of real sources, which may be either natural or man-made. These examples illustrate the wide range of spatial coherence states that may need to be measured. General measurement issues, which do not depend on the chosen method, are described in Sect. 3C. These considerations include the dimensionality of coherence functions that need to be measured. This depends on the type of the source. The amount of data to be measured depends, of course, on both the dimensionality of the problem and the required resolution.

Figure 3 illustrates the basic concepts related to spatial coherence, along with the notation to be used. For simplicity, we model the source as a field generated by a (generally three-dimensional) primary source across a plane O in front of the real source, and define a position at this plane by a transverse coordinate $\boldsymbol{\rho}$. The field across O is generally random, exhibiting phase, amplitude, and generally also polarization fluctuations at a time scale far too rapid to be followed without special techniques. The observable quantities are therefore statistical averages over the instantaneous properties of the field, described by means of correlation functions. These correlation functions evolve as the field propagates to a plane A at a distance D behind O, where the transverse coordinate is denoted by $\mathbf{r}$.

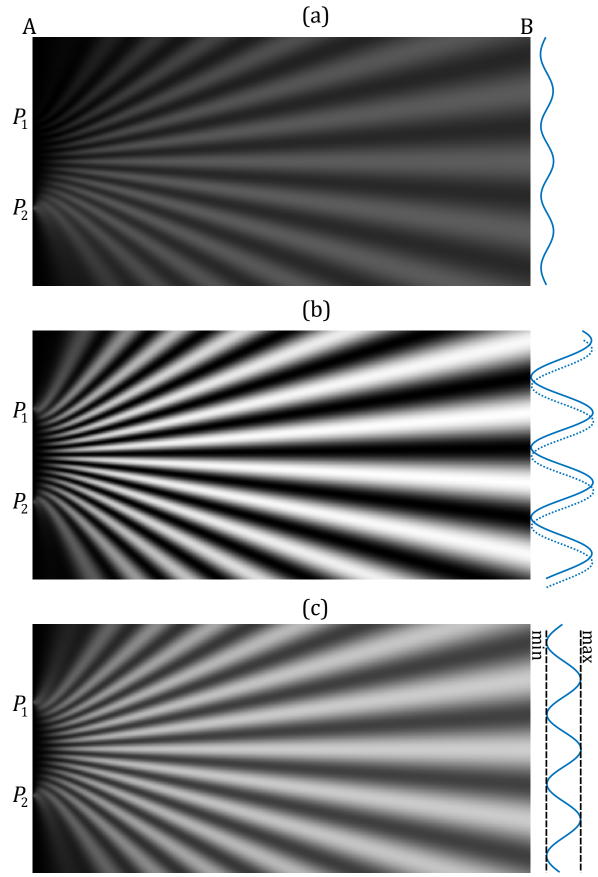

Fig. 2. Schematic illustration of interference in Young's two-pinhole experiment. The incident wave field is diffracted by pinholes P_1 and P_2 on screen A, and produces interference fringes on screen B. (a) Lowering the amplitude of P_1 with respect to P_2 causes the visibility to decrease. (b) Varying the phase at either pinhole causes the interference fringes to move laterally across screen B. (c) Partial coherence at screen A reduces the visibility of time-averaged interference fringes.

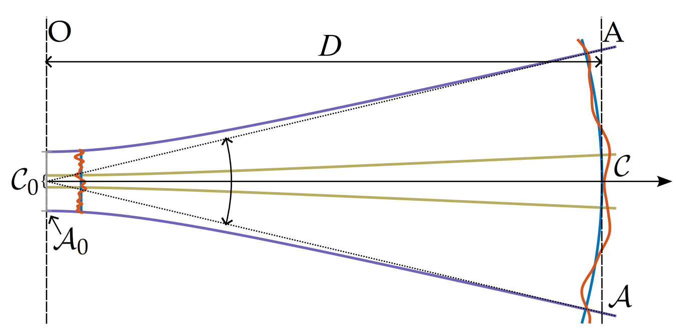

Fig. 3. Illustration of the effective size $\mathcal{A}_0$ and spatial coherence area $\mathcal{C}_0$ of the field in the source plane O, $\mathcal{C}_0$ being defined as the region where correlations between field fluctuations at positions $\boldsymbol{\rho}_1$ and $\boldsymbol{\rho}_2$ are significant. Corresponding areas at plane A are denoted by $\mathcal{A}$ and $\mathcal{C}$, respectively.

In particular, spatial coherence is described by considering correlations between fields at two spatial points, $\boldsymbol{\rho}_1$, and $\boldsymbol{\rho}_2$ at plane O, or $\mathbf{r}_1$, and $\mathbf{r}_2$ at A. With some reservations to be discussed later on, spatial coherence can be measured by observing the visibility of the interference fringes as outlined in Fig. 2. The coherence area $\mathcal{C}_0$ of the field at plane O is defined as the effective area over which fringes of appreciable contrast are observed on screen A. The radius of a circle that contains $\mathcal{C}_0$ can be used as a measure of coherence width.

In some scenarios the coherence area $\mathcal{C}_0$ is far smaller than the source area $\mathcal{A}_0$, in which case the field is called quasihomogeneous. This is the case, e.g., if we consider blackbody radiation emerging from an aperture at O. In fact, for such radiation $\mathcal{C}_0$ is in the wavelength scale, thus allowing us to treat the source as a nearly incoherent one. As the field propagates, $\mathcal{C}$ then grows linearly with the propagation distance D, as given by the van Cittert–Zernike theorem [13, 14]; see Sect. 4.4.4 of Ref. [2]. Nevertheless, due to its high divergence, the field remains quasi-homogeneous at all propagation distances D.

Depending on the source in question, the sizes $\mathcal{A}$ and $\mathcal{C}$ can be of the same order of magnitude, or we may have $\mathcal{C} \gg \mathcal{A}$, in which case the field is nearly spatially coherent. Generally, for a field radiated by a non-quasihomogeneous source, both $\mathcal{C}$ and $\mathcal{A}$ become nonlinear functions of distance D. In some cases, both may even decrease initially. However, at sufficiently large propagation distances D, they grow linearly. This is because the field in the far-zone (where $D \to \infty$) approximates a spherical wave emerging from an axial point $\boldsymbol{\rho}_0$, with a radius of curvature $R = D$. The field fluctuates on the surface of this sphere, and the fluctuations determine the correlation characteristic of the field on this sphere (see Sect. 5.3 of [2]. If we extract the spherical phase, we effectively obtain the field size $\mathcal{A}$ and the coherence area $\mathcal{C}$ across a far-zone observation plane A tangential to the sphere.

Examination of the relations between the source-plane coherence characteristics and those of propagated fields at any distance D (including the far-field) generally requires evaluation of propagation integrals of correlation functions. This can be done analytically only in a limited number of cases even in the far zone. Such analytical results can be obtained for any D if we consider so-called Gaussian Schell-model (GSM) fields, discussed in Sect. 4D. In the GSM the source-plane spatial coherence may vary continuously between incoherence and full coherence, and the model will help to quantify several features that we discuss here only in qualitative terms.

In certain circumstances it is possible to draw qualitative conclusions on the relations between source-plane and far-field characteristic in simple terms. This is true particularly if the field is quasihomogeneous at plane O. In this case the coherence width at O determines the beam divergence, which becomes inversely proportional to the source-plane coherence width. Conversely, the far-field coherence width becomes inversely proportional to the size of the source. The relations between source-plane coherence and beam divergence were studied rather extensively already in the 1970s. In particular, Wolf and Collett [22–24] showed, by considering GSM fields, that partially coherent sources of any state of coherence can have the same directionality as a fully coherent planar Gaussian source of certain well-defined spatial width. The field emitted by such an 'equivalent coherent source' can be considered as an effective (or 'elementary') field associated with the source. This spawned a lot of immediate interest [25–27]. In particular, Gori and Palma [28] showed that such an elementary-field description applies to GSM fields with any state of coherence, allowing one to represent the entire partially coherent field as a suitably weighted incoherent superposition of laterally shifted replicas of the elementary fields. They also introduced an alternative formulation, in which the effective coherent field has the same size as that of the entire partially coherent field at the source plane. In this model, the total partially coherent field can be represented as an incoherent angular superposition of the elementary fields.

The spatial coherence properties of light generally depend on the (angular) frequency of light, ω. This dependence is typically substantial and it cannot be ignored for broadband fields, such as blackbody radiation. To illustrate this point, we consider a particular example. In one of his seminal papers [3], Wolf investigated the coherence properties of planar quasihomogeneous sources that radiate light with the same (normalized) far-zone spectrum in every direction. He concluded that this is possible only if the degree of spatial coherence at plane O is a function of the form $h\left[\omega\left(\boldsymbol{\rho}_1 - \boldsymbol{\rho}_2\right)/c\right]$, where c is the speed of light in vacuum. When this condition is satisfied, the normalized far-field spectrum is the same as the normalized source-plane spectrum (which is assumed to be the same at every point $\boldsymbol{\rho}$). If it is not satisfied, correlation-induced spectral changes take place upon propagation, which can lead, e.g., to red (or blue) shifts in the spectrum [29, 30]. Examples of sources that satisfy the condition for spectral invariance include Lambertian sources, for which h is a sinc function.

Finally, the coherence and polarization properties of optical fields are in general coupled, and the full description requires an electromagnetic analysis. In the paraxial domain these properties can be described in a unified way by means of the 2×2 coherence-polarization matrices advocated by Wolf [4]; see also the related works of Gori in Refs. [31, 32]. These phenomena manifest also in the fringe visibility in Young's experiment. In particular, if the fields at pinholes P_1 and P_2 at plane A are orthogonally polarized, the contrast of the interference pattern vanishes even for fully spatially coherent illumination.

A. Examples of partially coherent fields

At this stage it seems useful to briefly discuss the spatial coherence properties of both natural and man-made light sources and fields they radiate, using simple heuristic arguments, to appreciate the requirements and challenges associated with measuring their spatial coherence properties. We proceed to qualitatively describe the main properties of several sources of practical interest.

Thermal sources emit broadband radiation with a spectrum that can be closely approximated by the blackbody spectrum. If, as is usual in microscopy, the field at plane O is generated with a Köhler condenser, the field inside an aperture $\mathcal{A}_0$ in O is effectively unpolarized and has a uniform intensity distribution at all frequencies. The spatial coherence is low and the spectral degree of spatial coherence satisfies Wolf's scaling law [3] with $h(u) = 2J_1(u)/u$, where J_1 is the Bessel function of order one, the argument is $u = (\omega/c)\left|\boldsymbol{\rho}_1 - \boldsymbol{\rho}_2\right|$ NA, and NA represents the numerical aperture of the condenser (see Sec. 10.5.3 in Ref. [1]).

Gas and solid-state lasers come in many forms with different spatial coherence properties. Lasers operating in a single transverse mode have high spatial coherence and low divergence. In multimode operation the spatial coherence is reduced, and can be low if the number of transverse modes is large (as is the case for, e.g., excimer lasers). Depending on the cavity, the radiation can be highly polarized or unpolarized. These lasers can produce either continuous-wave beams or trains of short pulses with a duration down to the sub-cycle regime.

Edge-emitting semiconductor lasers operating in a single spatial mode produce highly coherent and highly linearly polarized radiation, which however is anisotropic: the divergence differs in the two orthogonal directions since the source itself is anisotropic. In multimode operation the coherence is reduced according to the number of excited modes, which depends on the size of the emitting area [33, 34]. Usually the height of the emitting stripe is chosen to support only a single mode in a direction (say, y) perpendicular to the junction, in which case the coherence of the radiation is reduced only in the x direction.

Free-electron lasers (FELs) are large-scale facilities producing trains of intense pulses, with the time-averaged coherence properties varying rather widely according to the particular implementation [35]. Both spatial and temporal coherence of FEL radiation have been well-characterized experimentally [36–38]. Typically the beams generated by FELs are anisotropic, but their spatial coherence properties can often be described, at least approximately, by the Gaussian Schell model [39].

Light-emitting diodes (LEDs) are polychromatic sources that produce highly divergent and nearly unpolarized radiation. Thanks to the technological developments over the past two decades [40, 41], the brightness of LEDs has improved dramatically to the level that LEDs have rapidly replaced other sources in lighting applications. The spectra of 'monochromatic' LEDs is in the 10 nm region for visible light. However, the spectra can be made substantially wider (mimicking white light) if a part of the radiation from a blue LED is down-converted to the yellow region using phosphorous materials. The spatial coherence area of LEDs at the source plane is of the same order of magnitude as for thermal light, thus allowing them to be considered as quasihomogeneous sources. The exact form of the spectral degree of coherence can be retrieved from the radiation pattern. It satisfies Wolf's scaling law well for 'monochromatic' LEDs, and approximately also for 'white' LEDs [42].

Supercontinuum (SC) light can be generated in most bulk media using trains of intense pulses [43–45], or in optical fibers at substantially lower pump-pulse intensity [46]. SC is broadband, featuring spectra that can be multiple optical octaves wide [45, 47]. In bulk SC the divergence of the radiation depends on how tightly the pump field is focused, while in fiber SC it is defined by the output numerical aperture of the fiber. A recent simulation study [48] indicates, perhaps somewhat surprisingly, that the spatial coherence of bulk SC is high. Considering SC generation in single-spatial-mode fibers, spatial coherence is complete at each frequency. However, because the effective mode area depends on ω, the time-domain spatial coherence is not perfect [49], but it is nevertheless relatively high. In multimode fibers the spatial coherence depends on the number modes and their weights, but this subject remains to be studied in detail.

Fields with tailored coherence and polarization properties can be generated virtually from any field discussed above. The variety of techniques to accomplish this is too wide to be covered here, but the options include optical systems containing non-rotationally-symmetric elements, anisotropic or birefringent media, interferometers, and diffractive elements.

Many of the sources described above are nonstationary and produce trains of pulses, while 'slow' square-law detectors are almost exclusively used to measure spatial coherence. Such slow detectors typically average over many pulses in the train, in which case the measurements provide results analogous to those of stationary fields. We will justify this point more precisely in Sect. 7.

B. General measurement issues

In the geometry of Fig. 3 we measure coherence across a plane at a given distance D from the source plane. This distance is, of course, variable, but the size of the field increases with D until it may no longer fit within the aperture of the system. This can happen especially when we are in the far-zone region. However, as is well known from standard Fourier optics, the scaled version of the far-zone field can be observed at a chosen distance by placing the observation plane in the back focal plane of a Fourier transforming optical system [see Ref. [50], chapter 5]. In the case of polychromatic fields, such a system needs to be well color-corrected (preferably apochromatic).

In practice, the observation plane A cannot usually be the source plane O itself. In such a case, one can employ standard imaging systems to produce a secondary source at the image plane O′ of O. If the field is not substantially truncated by the aperture stop of the imaging system and the system is essentially aberration-free, the field dimensions and coherence properties at O′ are similar to those at O, except for a transverse scale given by the magnification m of the system. The use of imaging systems becomes particularly important when the degree of spatial coherence at O varies in wavelength-scale and therefore cannot be resolved with standard array detectors. Several practically relevant sources with such properties were already identified in the previous subsection. In terms of the Abbe theory of image formation, high-NA microscope objectives are needed to transmit at least most of the relevant spatial frequencies contained in the (highly divergent) field. Another related advantage of high transverse magnification is that it increases the effective depth of field, thus making it easier to place the input plane A of the measurement system at the plane O′. Further, the divergence of the magnified field decreases with m, with the output field becoming essentially paraxial at large values of m. In fact, it is sometimes convenient to construct the entire system (including both the coherence measurement instrument and the imaging setup) onto a single platform that can be moved as a whole in the z direction to study the properties of propagated fields.

If the spectrum of the field to be measured is narrow, a single spatial coherence measurement can be sufficient. In the case of broadband fields the spatial coherence typically becomes frequency-dependent and at least some spectral resolution is needed. On the other hand, especially if the polarization state of the field depends on position, with two-point spatial coherence and polarization phenomena becoming coupled, one needs polarization-sensitive measurement schemes. For beam-like fields, this implies that (at least) four coherence measurements using polarization-controlling systems are required, in analogy with analyzing the polarization state of partially polarized plane waves; see Sect. 6.2 of Ref. [2].

To obtain spectral resolution one may in principle use bandpass filters with different central frequencies (or wavelenghts) and select sufficiently narrow spectral samples from the incident field and to measure spatial coherence for each frequency band separately. A tunable Fabry–Perot filter is also an option, as is the use of dispersive elements (such as a prism or a grating). The latter approach, however, requires one dimension on the array detector for spectral resolution, therefore being applicable only if measurement of spatial coherence in the orthogonal direction is sufficient. Yet another option, which avoids sacrificing one spatial dimension, is to measure the full space-time correlation function, including an arbitrary time delay, which is in fact possible using some of the methods to be discussed.

In this scenario the space-frequency correlation properties can be obtained by means of the Wiener–Khintchine theorem (see Sect. 2.4.4 of Ref. [2]).

Considering practical issues, the data acquisition time required to perform coherence measurements depends critically on the type of instrument used, as does the light intensity level required to get the data at a sufficient signal-to-noise ratio (SNR), i.e. signal power divided by noise power. We therefore leave the discussion of these issues to later sections. Instead, we address here the dimensionality of the data that needs to be measured. This is independent of the method used, but rather depends on the properties of the source and whether we require spectral resolution or not.

In spectrally resolved spatial coherence measurements the required number Q of spectral samples depends on the width of the incident spectrum, but also on how rapidly it varies. For smooth spectra, such as the blackbody spectrum, $Q \sim 10 - 20$ may already be sufficient. If a dispersive element is used and the measurement setup is designed to fit the incident spectrum essentially over the detector area, Q can be as large as the number of pixels in the y direction (~ 1000).

From now on we assume that the spatial intensity of the incident field (or the spectral density at any desired frequency) can be measured, which is typically done by keeping only one channel of the measurement instrument open. Hence, it remains to consider the dimensionality of the spatial degree of coherence (DOC). If we only need to measure spatial coherence in one dimension (1D), the DOC data matrix is generally two-dimensional (2D). However, if the incident field obeys the Schell-model, i.e., if the DOC depends only on coordinate differences [51], the matrix becomes 1D in each direction and thus 2D if we need the DOC in both x and y directions. If the field is not of the Schell-model form, the dimensionality grows substantially and the spatial data matrix becomes four-dimensional (4D). Let us assume that we measure the DOC at $M \times N$ spatial points for (x_1, y_1) and $P \times R$ points for (x_2, y_2). In this general case we obtain a 4D matrix with $MNPR$ elements. Considering a normal laboratory computer with 16 GB of rapid-access memory and store the data in 8-bit form, the upper limit for the product $MNPR$ is approximately 1.3×10^{10}. Hence, if we set $M = N = P = R$, we get an upper bound $M \approx 336$. This applies to scalar field, but the data storage space required for electromagnetic measurements grows only by a factor of 4. If spectral resolution of Q samples is required, the matrix becomes five-dimensional (5D). Fortunately, depending on the source and also on the intended purpose of the spatial coherence measurements, we do not necessarily need the same number of samples in all four spatial directions. Sometimes it may, e.g., be sufficient to have only a few samples of (x_1, y_1), or to use high resolution only in one direction, which leads to three-dimensional (3D) spatial data matrices. One example of the former situation is determination of the mode structure of optical beams from spatial coherence measurements [52]. In conclusion, fast-access storage space is not usually a critical limiting issue.

4. YOUNG'S INTERFEROMETER

Let us return to the coherence measurement with Young's interferometer and describe the results in quantitative terms, starting with scalar analysis. Figure 4 illustrates the geometry and notation in detail. The pinholes at points $\mathbf{r}_1$ and $\mathbf{r}_2$ on screen A produce an interference pattern on screen B, located at a distance L behind screen A. As already mentioned above, this pattern is generally colored, and its local contrast around an arbitrary observation point $\mathbf{R}$ depends on the bandwidth of the incident field. An optional spectral filter F selects a certain spectral band around a reference frequency ω_0. Reducing the passband ω_F of F increases the local fringe contrast; in the quasimonochromatic limit $\omega_\mathrm{F} \ll \omega_0$ the fringe contrast depends only on field correlations between the pinholes, this being the initial assumption in standard textbooks [1, 2]. However, here we formulate the theory of Young's interferometer for incident fields with an arbitrary spectrum. To this end, it is convenient to start with the space-frequency field representation using the scalar theory.

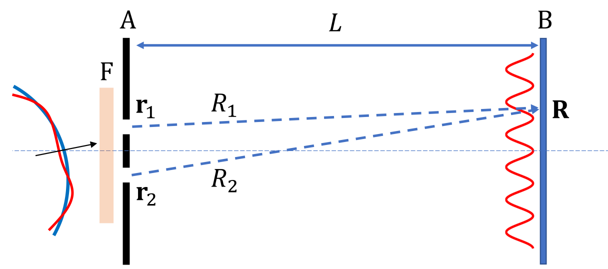

Fig. 4. Young's interferometer: geometry and notation. The red and blue curves represent the phase of an arbitrary field realization and the mean over all realizations, respectively, of the field approaching screen A.

A. Scalar formulation in the space-frequency domain

We denote an arbitrary spectral field realization (in the complex analytic signal representation) at point $\mathbf{r} = (x, y)$ on screen A, and at frequency ω, by $E(\mathbf{r}; \omega)$. The amplitudes and phases of these realizations are random. The phases fluctuate around a mean value $\phi(\mathbf{r}; \omega)$, illustrated in Fig. 4 with a blue curve. The mean wavefront may generally be aspherical, but for clarity a spherical wavefront is shown in Fig. 4. It is, however, deterministic by definition, allowing us to extract it by writing the field realizations in the form

$$E(\mathbf{r}; \omega) = E_0(\mathbf{r}; \omega) \exp\left[i\phi(\mathbf{r}; \omega)\right]. \tag{1}$$

We note that this representation is analogous to introducing a best-fitting reference sphere in the wave theory of aberrations [53]; in well-corrected optical systems the phase difference between the true aberrated wavefront and the reference sphere is in the sub-2π scale, while the phase difference between the reference sphere and the entrance pupil of the system may be orders of magnitude larger. We will see later on that representing the realizations as in Eq. (1) can be of substantial practical value in measurement of the phases of the associated correlation functions.

By introducing also a reference frequency ω_0, which can be, e.g., the peak or mean frequency of the spectrum of the field at A, the spectral dependence of the deterministic part of the wavefront has the form

$$\phi(\mathbf{r}; \omega) = \frac{\omega}{\omega_0} \phi(\mathbf{r}; \omega_0). \tag{2}$$

For quasimonochromatic fields centered at ω_0, this spectral dependence can essentially be ignored, but it is significant for broadband fields.

Spatial coherence properties of the field between two arbitrary points $\mathbf{r}_1$ and $\mathbf{r}_2$ at frequency ω are described by the cross-spectral density function (CSD)

$$W(\mathbf{r}_1, \mathbf{r}_2; \omega) = \langle E^*(\mathbf{r}_1; \omega) E(\mathbf{r}_2; \omega) \rangle \tag{3}$$

where the brackets and the asterisk denote ensemble averaging and complex conjugation, respectively. The spectral density of the field is defined as the equal-point CSD, $S(\mathbf{r};\omega) = W(\mathbf{r},\mathbf{r};\omega)$. It is customary to introduce a normalized quantity, known as the complex degree of coherence (DOC) in the space-frequency domain, by writing

$$\mu(\mathbf{r}_1,\mathbf{r}_2;\omega) = \frac{W(\mathbf{r}_1,\mathbf{r}_2;\omega)}{\sqrt{S(\mathbf{r}_1;\omega)S(\mathbf{r}_2;\omega)}} = |\mu(\mathbf{r}_1,\mathbf{r}_2;\omega)| \exp\left[i\alpha(\mathbf{r}_1,\mathbf{r}_2;\omega)\right], \tag{4}$$

where $\alpha(\mathbf{r}_1,\mathbf{r}_2;\omega)$ denotes the phase of $\mu(\mathbf{r}_1,\mathbf{r}_2;\omega)$. By applying Eqs. (1) and (2), we readily find that

$$W(\mathbf{r}_1,\mathbf{r}_2;\omega) = W_0(\mathbf{r}_1,\mathbf{r}_2;\omega) \times \exp\left\{i(\omega/\omega_0)\left[\phi(\mathbf{r}_2;\omega_0) - \phi(\mathbf{r}_1;\omega_0)\right]\right\}, \tag{5}$$

where $W(\mathbf{r}_1,\mathbf{r}_2;\omega) = \langle E_0^*(\mathbf{r}_1;\omega)E_0(\mathbf{r}_2;\omega)\rangle$.

Let us take the two pinholes in Young's setup to lie at transverse positions $\mathbf{r}_1 = (x_1, y_1)$ and $\mathbf{r}_2 = (x_2, y_2)$ on screen A as illustrated in Fig. 4. We assume that the pinholes are small enough for the phase of the mean wavefront (or of any individual realization) to be essentially constant across each pinhole, yet large enough for Kirchhoff's boundary conditions to hold. In these circumstances the diffracted fields at an arbitrary observation point $\mathbf{R} = (X, Y)$ on screen B are spherical waves expressible as

$$E(\mathbf{R};\omega) = (\omega/\omega_0)K_j E(\mathbf{r}_j;\omega)\exp(i\omega R_j/c), \tag{6}$$

where $K_j = -i\omega_0 A_j/2\pi c R_j$ with A_j being the area of the aperture at $\mathbf{r}_j$. In the paraxial region we may approximate $R_1 \approx R_2$ in the amplitude terms K_j, which gives $K_1 = K_2 = K_0$ (we assume $A_1 = A_2$), while in the phase factor in Eq. (6) the second-order Taylor approximation

$$R_j \approx L + \frac{(X - x_j)^2}{2L} + \frac{(Y - y_j)^2}{2L} \tag{7}$$

is needed.

With these notations and assumptions, the two-beam superposition field at point $\mathbf{R}$ can be expressed as

$$E(\mathbf{R};\omega) = (\omega/\omega_0)K_0 E(\mathbf{r}_1;\omega)\exp\left(i\omega R_1/c\right) + (\omega/\omega_0)K_0 E(\mathbf{r}_2;\omega)\exp\left(i\omega R_2/c\right). \tag{8}$$

We are interested in measuring the spectral interference pattern at point $\mathbf{R}$ on screen B, which is given by the spectral density

$$S(\mathbf{R};\omega) = \langle E^*(\mathbf{R};\omega)E(\mathbf{R};\omega)\rangle = \langle |E(\mathbf{R};\omega)|^2\rangle. \tag{9}$$

Inserting from Eq. (8) and using Eq. (5) we obtain

$$S(\mathbf{R};\omega) = (\omega/\omega_0)^2 |K_0|^2 \left\{S(\mathbf{r}_1;\omega) + S(\mathbf{r}_2;\omega) + 2\Re\left[W_0(\mathbf{r}_1,\mathbf{r}_2;\omega)\exp[i(\omega/\omega_0)\phi(\mathbf{r}_1,\mathbf{r}_2;\omega_0)]\right]\right\}. \tag{10}$$

where $\Re$ denotes the real part and

$$\phi(\mathbf{r}_1,\mathbf{r}_2;\omega_0) = \phi(\mathbf{r}_2;\omega_0) - \phi(\mathbf{r}_1;\omega_0) + (R_2 - R_1)\,\omega_0/c. \tag{11}$$

Using Eq. (7) we have

$$R_2 - R_1 = \frac{(x_1 - x_2)\,X}{L} + \frac{(y_1 - y_2)\,Y}{L}, \tag{12}$$

where only the terms linear in X and Y have been retained as this is sufficient for our purposes. We may readily express the spectral interference law in Eq. (10) in the alternative form

$$S(\mathbf{R};\omega) = (\omega/\omega_0)^2 |K_0|^2 \Big\{S(\mathbf{r}_1;\omega) + S(\mathbf{r}_2;\omega) + 2\sqrt{S(\mathbf{r}_1;\omega)S(\mathbf{r}_2;\omega)}\,|\mu_0(\mathbf{r}_1,\mathbf{r}_2;\omega)| \times \cos\left[\alpha_0(\mathbf{r}_1,\mathbf{r}_2;\omega) + (\omega/\omega_0)\phi(\mathbf{r}_1,\mathbf{r}_2;\omega_0)\right]\Big\}, \tag{13}$$

where $|\mu_0(\mathbf{r}_1,\mathbf{r}_2;\omega)|$ and $\alpha_0(\mathbf{r}_1,\mathbf{r}_2;\omega)$ are the absolute value and phase of the spectral DOC associated with the random part of the incident field.

To see how the amplitude and phase of the spectral DOC can be determined from the interference pattern we assume (without truly sacrificing generality) that the pinholes are located on the x axis in screen A and the observation point is on the X axis in plane B. The oscillating part of the interference term in Eq. (13) is proportional to

$$M(X;\omega) = |\mu_0(x_1,x_2;\omega)| \cos\left\{\alpha_0(x_1,x_2;\omega) + (\omega/\omega_0) \times \left[\phi(x_2;\omega_0) - \phi(x_1;\omega_0) + (\omega_0/c)\,(x_2 - x_1)\,X/L\right]\right\}, \tag{14}$$

which is also referred to as the normalized interference pattern later on. The function $M(X;\omega)$ varies periodically, with period $\Lambda(x_1,x_2;\omega)$ given by

$$\frac{2\pi}{\Lambda(x_1,x_2;\omega)} = \frac{\omega_0}{c}\frac{|x_1 - x_2|}{L}, \tag{15}$$

between maxima $|\mu_0(x_1,x_2;\omega)|$ and minima $-|\mu_0(x_1,x_2;\omega)|$ as the observation point moves along the X axis. The entire interference pattern given by Eq. (13) therefore has maxima $S_{\max}(\omega)$ and minima $S_{\min}(\omega)$, which have the same values across the interference pattern. Defining the visibility of the spectral interference fringes as

$$V(\mathbf{R};\omega) = \frac{S_{\max}(\omega) - S_{\min}(\omega)}{S_{\max}(\omega) + S_{\min}(\omega)}, \tag{16}$$

we get a relation

$$V(X;\omega) = \frac{2\sqrt{S(x_1;\omega)S(x_2;\omega)}}{S(x_1;\omega) + S(x_2;\omega)}\,|\mu_0(x_1,x_2;\omega)| \tag{17}$$

between the observed fringe visibility and absolute value of the spectral DOC. Therefore we can determine $|\mu_0(x_1,x_2;\omega)|$ at any single frequency ω directly from the visibility measurements.

If the random part $\alpha_0(x_1,x_2;\omega)$ of the phase is zero, the expression (14) becomes symmetric about the equal-phase point

$$X_0 = \frac{L}{(\omega_0/c)\,(x_2 - x_1)}\left[\phi(x_1;\omega_0) - \phi(x_2;\omega_0)\right], \tag{18}$$

which is the same at all frequencies. If $\alpha_0(x_1,x_2;\omega) \neq 0$, the fringes shift laterally by a corresponding distance, as illustrated in Fig. 5. The shift generally depends on ω, but the phase $\alpha_0(x_1,x_2;\omega)$ can always be determined from it: at any ω a fringe shift of one period corresponds to a 2π phase change. The frequency dependence of the period $\Lambda(x_1,x_2;\omega)$, given by Eq. (15) and illustrated by the blue line in Fig. 5, can be ignored only for narrow-band fields. This turns out to be at the root of the fundamental problems on determining the time-domain spatial coherence properties of broadband fields.

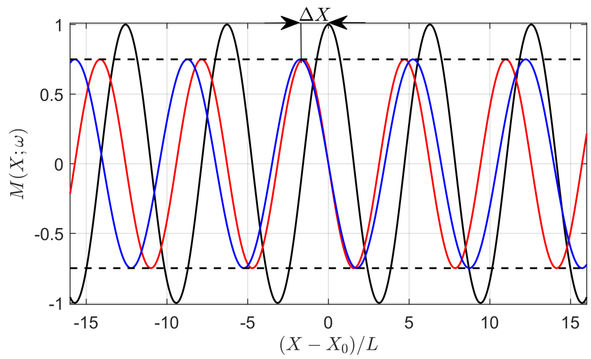

Fig. 5. Illustration of the oscillating term $M(X;\omega)$ in Young's interference experiment as a function of $(X - X_0)/L$, where X_0 is the equal-phase point. The black line represents the result at $\omega = \omega_0$ when $\mu_0(x_1, x_2;\omega) = 1$ and $\alpha_0(x_1, x_2;\omega) = 0$, while the red line corresponds to the value of the pinhole separation $x_2 - x_1$ that gives $\mu_0(x_1, x_2;\omega) = 0.75$ and $\alpha_0(x_1, x_2;\omega) = \pi/2$. The blue line is the same as the red one, but plotted at frequency $\omega = 0.9\omega_0$.

B. Scalar formulation in the space-time domain

We proceed to analyze Young's interference experiment in the space-time domain, which is indeed a more usual starting point [1, 2]. The spatio-temporal coherence properties of a random field can be analyzed by first Fourier-transforming the spectral field representation to obtain the corresponding space-time field according to

$$E(\mathbf{r};t) = \int_0^\infty E(\mathbf{r};\omega)\exp(-i\omega t)\,\mathrm{d}\omega, \tag{19}$$

where the lower bound of zero arises because we employ the complex analytic-signal representation. In the space-time domain we are interested in measuring the second-order field correlations that are described by the mutual coherence function (MCF), defined as an ensemble average over the temporal field realizations given by Eq. (19):

$$\Gamma(\mathbf{r}_1, \mathbf{r}_2;\Delta t) = \langle E^*(\mathbf{r}_1;t)E(\mathbf{r}_2;t+\Delta t)\rangle, \tag{20}$$

where $\Delta t = t_2 - t_1$ represents the difference between two arbitrary instants of time. Note that since we consider mainly statistically stationary fields that are ergodic, the ensemble average is equal to time average. That is, performing the ensemble average produces a correlation function that is invariant in the $t = (t_1 + t_2)/2$ direction, and any slice along the Δt coordinate completely characterizes the temporal correlations. This is no longer true for statistically nonstationary (pulsed) fields, although the time-averaged spatial coherence measurements are applicable in that case as well, as we will demonstrate in Sect. 7.

Spatial correlations are characterized by the equal-time MCF, $\Gamma(\mathbf{r}_1, \mathbf{r}_2;0)$, while the intensity of the field, given by $I(\mathbf{r}) = \Gamma(\mathbf{r}, \mathbf{r};0)$, is constant at every point. The time-domain DOC is defined, in analogy with Eq. (4), as

$$\begin{aligned}\gamma(\mathbf{r}_1, \mathbf{r}_2;\Delta t) &= \frac{\Gamma(\mathbf{r}_1, \mathbf{r}_2;\Delta t)}{\sqrt{I(\mathbf{r}_1)I(\mathbf{r}_2)}}\\ &= |\gamma(\mathbf{r}_1, \mathbf{r}_2;\Delta t)|\exp\left[i\delta(\mathbf{r}_1, \mathbf{r}_2;\Delta t)\right],\end{aligned} \tag{21}$$

where $\delta(\mathbf{r}_1, \mathbf{r}_2;\Delta t)$ denotes the phase. Generally, the MCF and the CSD are related by the Wiener–Khintchine theorem (Ref. [2], Sect. 2.4.4)

$$\Gamma(\mathbf{r}_1, \mathbf{r}_2;\Delta t) = \int_0^\infty W(\mathbf{r}_1, \mathbf{r}_2;\omega)\exp(-i\omega\Delta t)\,\mathrm{d}\omega. \tag{22}$$

This theorem implies that if we are concerned with spatial coherence in the time domain, we only need to integrate the CSD over all frequencies to obtain the zero-delay MCF

$$\Gamma(\mathbf{r}_1, \mathbf{r}_2;0) = \int_0^\infty W(\mathbf{r}_1, \mathbf{r}_2;\omega)\mathrm{d}\omega. \tag{23}$$

Further, the temporal intensity and the spectral density are related by

$$I(\mathbf{r}) = \int_0^\infty S(\mathbf{r};\omega)\mathrm{d}\omega, \tag{24}$$

i.e., the temporal intensity at any point is equal to the frequency-integrated spectral density.

We can determine the time-domain interference pattern starting from the spectral interference pattern in Eq. (10) and applying Eq. (24). Doing so, we obtain the result

$$\begin{aligned}I(\mathbf{R}) = &|K_0|^2\int_0^\infty(\omega/\omega_0)^2\left[S(\mathbf{r}_1;\omega) + S(\mathbf{r}_2;\omega)\right]\mathrm{d}\omega\\ &+ 2|K_0|^2\,\Re\int_0^\infty(\omega/\omega_0)^2\left[W_0(\mathbf{r}_1, \mathbf{r}_2;\omega)\right.\\ &\left.\times\exp\left[i(\omega/\omega_0)\phi(\mathbf{r}_1, \mathbf{r}_2;\omega_0)\right]\right]\mathrm{d}\omega.\end{aligned} \tag{25}$$

Although the factor ω/ω_0 inside the integrals varies relatively slowly, it cannot be ignored if we consider broadband fields with, e.g., Planck, supercontinuum, or white-LED spectra. If the spectrum is sufficiently narrow for us to ignore this factor, the first line of Eq. (25) becomes proportional to the sum of intensities generated when only one pinhole is open. The time-domain interference pattern in Eq. (25) can then be cast into the form

$$\begin{aligned}I(\mathbf{R}) = &|K_0|^2\left[I(\mathbf{r}_1) + I(\mathbf{r}_2)\right]\\ &+ 2|K_0|^2\int_0^\infty\sqrt{S(\mathbf{r}_1;\omega)S(\mathbf{r}_2;\omega)}\,|\mu_0(\mathbf{r}_1, \mathbf{r}_2;\omega)|\\ &\times\cos[\alpha_0(\mathbf{r}_1, \mathbf{r}_2;\omega) + (\omega/\omega_0)\phi(\mathbf{r}_1, \mathbf{r}_2;\omega_0)]\,\mathrm{d}\omega.\end{aligned} \tag{26}$$

However, we cannot ignore the ω dependence inside the argument of the exponential term in Eq. (25). As already seen, the presence of this factor makes the period of the spectral interference pattern strongly frequency-dependent.

As already pointed out, the time-domain interference fringes produced by Young's interferometer become colored and lose contrast when polychromatic light is considered, even though at least some fringes can still be seen even for white light. It follows directly from Eq. (26) that

$$\begin{aligned}I(\mathbf{R}) = |K_0|^2\Big\{&I(\mathbf{r}_1) + I(\mathbf{r}_2) + 2\sqrt{I(\mathbf{r}_1)I(\mathbf{r}_2)}\\ &\times|\gamma_0(\mathbf{r}_1, \mathbf{r}_2;\Delta t_\mathbf{R})|\cos\left[\delta_0(\mathbf{r}_1, \mathbf{r}_2;\Delta t_\mathbf{R})\right]\Big\},\end{aligned} \tag{27}$$

where $\Delta t_\mathbf{R} = \phi(\mathbf{r}_1, \mathbf{r}_2;\omega_0)/\omega_0$ is a position-dependent time delay. Measurements around the equal-time point $\mathbf{R}$ at a position where $\Delta t_\mathbf{R} = 0$ would then, in a formal sense, give precisely the time-domain degree of spatial coherence $\gamma_0(\mathbf{r}_1, \mathbf{r}_2;0)$ of the random part of the field, which is the quantity we are looking for. However, as we will demonstrate by simulations in Sect. 4E, unambiguous experimental measurements of this quantity requires that the spectrum has a sufficiently narrow effective bandwidth, i.e., that the incident field is essentially quasimonochromatic.

C. Electromagnetic formulation

The scalar analysis of Young's interferometer presented in the previous section is satisfactory for paraxial (or beam-like) incident fields, for which the vectorial nature can be largely ignored as long as the state of polarization across screen A is uniform. In such circumstances the x and y components of the vector field $\mathbf{E}(\mathbf{r};\omega)$ decouple on propagation and can therefore be analysed within scalar theory, while the z component is negligible. In general, however, the polarization state of $\mathbf{E}(\mathbf{r};\omega)$ may depend on both $\mathbf{r}$ and ω, which necessitates a vectorial analysis of the results of Young's interferometer, as well as any other coherence measurement method.

The (transverse) electric vector of the beam incident on Young's interferometer may be defined by a column vector $\mathbf{E}(\mathbf{r};\omega) = [E_x(\mathbf{r};\omega), E_y(\mathbf{r};\omega)]^{\mathrm{T}}$ where $E_x(\mathbf{r};\omega)$ and $E_y(\mathbf{r};\omega)$ are the Cartesian field components and T denotes the transpose. In analogy to Eq. (1) in the scalar case, we extract the deterministic part of the phase front as

$$\mathbf{E}(\mathbf{r};\omega) = \mathbf{E}_0(\mathbf{r};\omega)\exp\left[i\phi(\mathbf{r};\omega)\right], \tag{28}$$

with $\phi(\mathbf{r};\omega)$ given in Eq. (2). The interference field on the observation screen thus takes the form

$$\begin{aligned}\mathbf{E}(\mathbf{R};\omega) &= (\omega/\omega_0)K_0\mathbf{E}(\mathbf{r}_1;\omega)\exp\left(i\omega R_1/c\right)\\ &+ (\omega/\omega_0)K_0\mathbf{E}(\mathbf{r}_2;\omega)\exp\left(i\omega R_2/c\right).\end{aligned} \tag{29}$$

The polarimetric characteristics are traditionally described in terms of the (polarization or one-point) Stokes parameters defined as [2]

$$S_0(\mathbf{r};\omega) = \Phi_{xx}(\mathbf{r};\omega) + \Phi_{yy}(\mathbf{r};\omega), \tag{30}$$

$$S_1(\mathbf{r};\omega) = \Phi_{xx}(\mathbf{r};\omega) - \Phi_{yy}(\mathbf{r};\omega), \tag{31}$$

$$S_2(\mathbf{r};\omega) = \Phi_{xy}(\mathbf{r};\omega) + \Phi_{yx}(\mathbf{r};\omega), \tag{32}$$

$$S_3(\mathbf{r};\omega) = i\left[\Phi_{yx}(\mathbf{r};\omega) - \Phi_{xy}(\mathbf{r};\omega)\right], \tag{33}$$

where $\Phi_{ij}(\mathbf{r};\omega) = \langle E_i^*(\mathbf{r};\omega)E_j(\mathbf{r};\omega)\rangle$, with $(i,j)\in(x,y)$, are the elements of the polarization matrix. The first parameter $S_0(\mathbf{r};\omega)$ is the spectral density, while $S_1(\mathbf{r};\omega), S_2(\mathbf{r};\omega), S_3(\mathbf{r};\omega)$ express the polarization state. With straightforward steps, the Stokes parameters related to field $\mathbf{E}(\mathbf{R};\omega)$ above, are found to be

$$\begin{aligned}S_n(\mathbf{R};\omega) &= |K_0|^2(\omega/\omega_0)^2\left\{S_n(\mathbf{r}_1;\omega) + S_n(\mathbf{r}_2;\omega)\right.\\ &\left.+ 2\Re\left[\mathcal{S}_{0,n}(\mathbf{r}_1,\mathbf{r}_2;\omega)\exp[i(\omega/\omega_0)\phi(\mathbf{r}_1,\mathbf{r}_2;\omega_0)]\right]\right\}.\end{aligned} \tag{34}$$

with $n\in(0,\ldots,3)$ and $\phi(\mathbf{r}_1,\mathbf{r}_2;\omega_0)$ given in Eq. (11). Further, $\mathcal{S}_{0,n}(\mathbf{r}_1,\mathbf{r}_2;\omega)$ are the (two-point) coherence Stokes parameters at the pinholes, explicitly given by [54–57]

$$\mathcal{S}_{0,0}(\mathbf{r}_1,\mathbf{r}_2;\omega) = W_{0,xx}(\mathbf{r}_1,\mathbf{r}_2;\omega) + W_{0,yy}(\mathbf{r}_1,\mathbf{r}_2;\omega), \tag{35}$$

$$\mathcal{S}_{0,1}(\mathbf{r}_1,\mathbf{r}_2;\omega) = W_{0,xx}(\mathbf{r}_1,\mathbf{r}_2;\omega) - W_{0,yy}(\mathbf{r}_1,\mathbf{r}_2;\omega), \tag{36}$$

$$\mathcal{S}_{0,2}(\mathbf{r}_1,\mathbf{r}_2;\omega) = W_{0,xy}(\mathbf{r}_1,\mathbf{r}_2;\omega) + W_{0,yx}(\mathbf{r}_1,\mathbf{r}_2;\omega), \tag{37}$$

$$\mathcal{S}_{0,3}(\mathbf{r}_1,\mathbf{r}_2;\omega) = i\left[W_{0,yx}(\mathbf{r}_1,\mathbf{r}_2;\omega) - W_{0,xy}(\mathbf{r}_1,\mathbf{r}_2;\omega)\right]. \tag{38}$$

Above, $W_{0,ij} = \langle E_{0,i}^*(\mathbf{r}_1;\omega)E_{0,j}(\mathbf{r}_2;\omega)\rangle$, with $(i,j)\in(x,y)$, are the elements of the cross-spectral density matrix associated with the field $\mathbf{E}_0(\mathbf{r};\omega)$.

We introduce the normalized coherence Stokes parameters via

$$\mu_{0,n}(\mathbf{r}_1,\mathbf{r}_2;\omega) = \frac{\mathcal{S}_{0,n}(\mathbf{r}_1,\mathbf{r}_2;\omega)}{\sqrt{S_0(\mathbf{r}_1;\omega)S_0(\mathbf{r}_2;\omega)}},\quad n\in(0,\ldots,3), \tag{39}$$

which may be viewed as the electromagnetic analogs of the complex degree of coherence of scalar fields defined in Eq. (4). Invoking the representation $\mu_{0,n}(\mathbf{r}_1,\mathbf{r}_2;\omega) = |\mu_{0,n}(\mathbf{r}_1,\mathbf{r}_2;\omega)|\exp[i\alpha_{0,n}(\mathbf{r}_1,\mathbf{r}_2;\omega)]$, enables us to write Eq. (34) as

$$\begin{aligned}S_n(\mathbf{R};\omega) &= |K_0|^2(\omega/\omega_0)^2\left\{S_n(\mathbf{r}_1;\omega) + S_n(\mathbf{r}_2;\omega)\right.\\ &+ 2\sqrt{S_0(\mathbf{r}_1;\omega)S_0(\mathbf{r}_2;\omega)}|\mu_{0,n}(\mathbf{r}_1,\mathbf{r}_2;\omega)|\\ &\left.\times\cos\left[\alpha_{0,n}(\mathbf{r}_1,\mathbf{r}_2;\omega) + (\omega/\omega_0)\phi(\mathbf{r}_1,\mathbf{r}_2;\omega_0)\right]\right\}.\end{aligned} \tag{40}$$

Due to the cosine term, the Stokes parameters exhibit (quasi) periodic oscillations with the local maxima and minima around $\mathbf{R}$ denoted by $S_{n,\max}(\omega)$ and $S_{n,\min}(\omega)$, respectively. The related visibilities are found to be

$$V_n(\mathbf{R};\omega) = \frac{2\sqrt{S_0(\mathbf{r}_1;\omega)S_0(\mathbf{r}_2;\omega)}}{S_0(\mathbf{r}_1;\omega)+S_0(\mathbf{r}_2;\omega)}\,|\mu_{0,n}(\mathbf{r}_1,\mathbf{r}_2;\omega)|. \tag{41}$$

This indicates that the magnitudes $|\mu_{0,n}(\mathbf{r}_1,\mathbf{r}_2;\omega)|$ of the normalized coherence Stokes parameters can be obtained from the visibility measurements, while the phases $\alpha_{0,n}(\mathbf{r}_1,\mathbf{r}_2;\omega)$ are found from the locations of the Stokes-parameter patterns.

We may define the degree of coherence of an electromagnetic beam by considering the visibility of the intensity fringes as in the scalar case or assessing the contrasts of both the intensity and polarization Stokes-parameter fringes. Assuming the same intensity in the pinholes, the degree of coherence related to the former case is $\mu_{0,n}(\mathbf{r}_1,\mathbf{r}_2;\omega)$ [4], whereas in the latter situation the degree (in squared form) is defined as [58, 59]

$$\mu^2(\mathbf{r}_1,\mathbf{r}_2;\omega) = \frac{1}{2}\sum_{n=0}^{3}|\mu_{0,n}(\mathbf{r}_1,\mathbf{r}_2;\omega)|^2, \tag{42}$$

where the factor $1/2$ ensures that $0\le\mu(\mathbf{r}_1,\mathbf{r}_2;\omega)\le 1$. Unlike the mere intensity-based measure of $\mu_{0,n}(\mathbf{r}_1,\mathbf{r}_2;\omega)$, the quantity $\mu(\mathbf{r}_1,\mathbf{r}_2;\omega)$ is purely real.

The electromagnetic formulation in the time domain is a straightforward extension of that in the scalar case. The limitations of Young's interferometer remain the same.

D. Example: polychromatic Gaussian Schell-model fields

Let us depart briefly from the discussion of Young's interferometer by introducing a specific model for partially coherent light, namely the Gaussian Schell model (GSM); see, e.g., Ref. [60]. Largely due to its mathematical simplicity, this is by far the most widely used model for partially coherent light, though it covers only one class of fields. In particular, the GSM allows us to quantify the concepts already introduced qualitatively in Sect. 3. This model can be used to illustrate measurement results with any of the techniques described below, not just Young's interferometer.

Specifically, we assume that the CSD of the field at the entrance plane of the measurement setup is of the separable form

$$W(x_1,y_1,x_2,y_2;\omega) = W(x_1,x_2;\omega)W(y_1,y_2;\omega), \tag{43}$$

where the x-dependent factor is

$$W(x_1,x_2;\omega) = W_0(x_1,x_2;\omega)\exp\left[i\phi(x_1,x_2;\omega)\right] \tag{44}$$

and a similar expression applies to the y-dependent factor. The random part of the CSD in Eq. (44) is given by

$$\begin{aligned}W_0(x_1,x_2;\omega) &= \sqrt{S_0(\omega)}\\ &\times\exp\left[-\frac{x_1^2+x_2^2}{w^2(\omega)}\right]\exp\left[-\frac{(x_1-x_2)^2}{2\sigma^2(\omega)}\right],\end{aligned} \tag{45}$$

where $S_0(\omega)$ represents the axial spectral density of the field. The (deterministic) phase factor in Eq. (44), which arises from the phase term in Eq. (1), has the form

$$\phi(x_1, x_2; \omega) = -\frac{\omega}{2cR(\omega)}(x_1^2 - x_2^2). \tag{46}$$

It can be readily established that $w(\omega)$ is the $1/e^2$ half-width of the (Gaussian) transverse profile $S(x;\omega) = W(x, x; \omega)$, $\sigma(\omega)$ is the rms half-width of the (Gaussian and real-valued) distribution $\mu_0(x_1, x_2; \omega)$, and $R(\omega)$ is the (paraxial-domain) radius of curvature of the incident wavefront. The random part of the CSD is clearly of the Schell-model form, as its spectral DOC depends only on the coordinate difference $x_2 - x_1$.

Even though strictly analogous expressions can be written for $W(y_1, y_2; \omega)$, it is worth considering a slight extension of the model. Generally both the beam width and the coherence width may be different in the two directions, i.e., $w_x(\omega) \neq w_y(\omega)$ and $\sigma_x(\omega) \neq \sigma_y(\omega)$, in which case the field is called anisotropic [61]. In general we also have $R_x(\omega) \neq R_y(\omega)$. In this case the field can be called astigmatic.

Gaussian Schell-model fields can be generated in various ways. A fairly standard laboratory technique is to start from a spatially coherent field, such as an isotropic or anisotropic Gaussian laser beam or pulse train, and then reduce the spatial coherence by passing the beam through a rotating diffuser [62]. One can (optionally) use a Gaussian apodizing filter to control the beam width at the measurement plane as, e.g., in Ref. [63].

The axial spectrum $S_0(\omega)$ can be of any form, but often it can be modelled by a Gaussian function

$$S_0(\omega) = S_0 \exp\left[-\frac{2\left(\omega - \omega_0\right)^2}{\Omega_0^2}\right], \tag{47}$$

where the parameter Ω_0 is a measure of the spectral bandwidth. This form is appropriate for, e.g., short optical pulses generated in spherical-mirror laser resonators. The field becomes quasi-monochromatic when $\Omega_0 \ll \omega_0$.

The parameters $w(\omega)$, $\sigma(\omega)$, and $R(\omega)$ generally depend on frequency and evolve on propagation according to simple laws, thus being often called the propagation parameters of the GSM beam [64]. Denoting by z the propagation distance from the 'waist' of the beam, where $w(\omega)$ and $\sigma(\omega)$ reach their minimum values $w_0(\omega)$ and $\sigma_0(\omega)$, respectively, and $R(\omega) = \infty$ (planar wavefront), these laws can be written as

$$w(\omega) = w_0(\omega)\left[1 + \frac{z^2}{z_\mathrm{R}^2(\omega)}\right]^{1/2}, \tag{48}$$

$$\sigma(\omega) = \sigma_0(\omega)\left[1 + \frac{z^2}{z_\mathrm{R}^2(\omega)}\right]^{1/2}, \tag{49}$$

$$R(\omega) = z + \frac{z_\mathrm{R}^2(\omega)}{z}. \tag{50}$$

Here we have denoted the so-called Rayleigh range of the beam by

$$z_\mathrm{R}(\omega) = \frac{1}{2}\frac{\omega}{c}w_0^2(\omega)\beta(\omega) \tag{51}$$

where

$$\beta(\omega) = \left[1 + \frac{w_0^2(\omega)}{\sigma_0^2(\omega)}\right]^{-1/2}. \tag{52}$$

In the limit of complete spatial coherence $\sigma_0(\omega) \to \infty$, $\beta(\omega) \to 1$, and $z_\mathrm{R}(\omega)$ reduces to the usual Rayleigh range of a Gaussian beam. In the case of a quasihomogeneous field with $\sigma_0(\omega) \ll w_0(\omega)$ we can approximate $\beta(\omega) \approx \sigma_0(\omega)/w_0(\omega)$. We finally note that the propagation parameters defined above can also be used to characterize GSM beams at the output plane of any paraxial optical system [65–67].

The formulas for the propagation parameters allow us to estimate the distance D from the beam waist (assumed to be at the plane O in Fig. 3) to the plane A such that the far-field conditions are fulfilled. The criterion $z \gg z_\mathrm{R}(\omega)$ leads to asymptotic results $w(\omega) \to w_0(\omega)z/z_\mathrm{R}(\omega)$, $\sigma(\omega) \to \sigma_0(\omega)z/z_\mathrm{R}(\omega)$, and $R(\omega) \to z$. The directionality of the radiation can now be characterized by the far-field diffraction angle

$$\Theta(\omega) = \lim_{z\to\infty}\frac{w(\omega)}{z} = \frac{2c}{\omega w_0(\omega)\beta(\omega)} \approx \frac{2c}{\omega\sigma_0(\omega)}. \tag{53}$$

Correspondingly, the angular coherence width is characterized by

$$\Sigma(\omega) = \lim_{z\to\infty}\frac{\sigma(\omega)}{z} = \frac{\sigma_0(\omega)2c}{\omega w_0^2(\omega)\beta(\omega)} \approx \frac{2c}{\omega w_0(\omega)}. \tag{54}$$

In both cases the approximate forms apply to the quasihomogeneous case, in which the directionality of the field is inversely proportional to the source-plane coherence width, while the angular coherence width is inversely proportional to the beam width at the source plane.

It is clear from Eq. (53) that all sources with an equal value of the product $w_0(\omega)\beta(\omega)$ radiate beams with the same directionality. If we compare an arbitrary GSM source with a fully coherent Gaussian source (an elementary source) of width $w_0(\omega) = w_\mathrm{E}(\omega)$, this condition leads to an equivalence relation [22, 68]

$$\frac{1}{w_\mathrm{E}^2(\omega)} = \frac{1}{w_0^2(\omega)} + \frac{1}{\sigma_0^2(\omega)}. \tag{55}$$

As shown in [28], an incoherent superposition of laterally shifted replicas of the 'elementary' source fields leads to a GSM source if the replicas are weighted by a suitable Gaussian function. On the other hand, if we consider anisotropic GSM sources, the condition

$$w_{0x}^2(\omega)\beta_x(\omega) = w_{0y}^2(\omega)\beta_y(\omega) \tag{56}$$

ensures that the ratio $w_x(\omega)/w_y(\omega)$ remains constant at all propagation distances including the far zone [69]. Hence fields that satisfy this condition may be called shape-invariant (at frequency ω).

To complete this subsection, we illustrate the spectral dependence of the propagation parameters of GSM beams by means of a particular example. In multimode operation, usual spherical-mirror laser resonators generate Hermite–Gaussian (HG) modes, which all have the same frequency-independent Rayleigh range $z_\mathrm{R}(\omega) = z_\mathrm{R}(\omega_0)$; see Chapt. 8 in Ref [70]. It then follows that the spatial width $w_\mathrm{HG}(\omega)$ of any HG mode, and any incoherent superposition of such modes, scales in frequency as

$$w_\mathrm{HG}(\omega) = \sqrt{\frac{\omega_0}{\omega}}w_\mathrm{HG}(\omega_0). \tag{57}$$

If the weights of the HG modes follow a certain exponential distribution [26, 71], the incoherent superposition of modes is a GSM beam, where the parameter $\beta(\omega) = \beta$ is independent of frequency. Explicitly, the CSD can in this case be written as [72]

$$W(x_1, x_2; \omega) = \sum_{m=0}^{\infty} c_m \psi_m^*(x_1; \omega) \psi_m(x_2; \omega), \tag{58}$$

where

$$c_m = w_{\mathrm{HG}}(\omega_0) \sqrt{\frac{2\pi}{\beta}} \frac{1}{1 + 1/\beta} \left(\frac{1-\beta}{1+\beta} \right)^m \tag{59}$$

and $\psi_m(x; \omega)$ denotes a HG mode of order m. The resulting GSM beam has a width $w(\omega) = w_{\mathrm{HG}}(\omega)/\sqrt{\beta}$, which scales spectrally as in Eq. (57), and also the coherence width given by

$$\sigma(\omega) = \frac{\sigma(\omega_0)}{w(\omega_0)} w(\omega) = \frac{\omega_0}{\omega} \sigma(\omega_0) \tag{60}$$

scales similarly. Finally, since the Rayleigh range is frequency-independent, so is the radius of wavefront curvature, i.e. $R(\omega) = R(\omega_0)$. In fact, when the spectral dependence of the transverse scale is of the form of Eq. (57), the multimode field becomes shape-invariant at all frequencies [73]. The same applies to anisotropic fields that satisfy Eq. (56).

E. Experimental considerations and limitations

To illustrate the problems in measuring the time-domain coherence of polychromatic fields with Young's interferometer more quantitatively, we consider some simple but representative simulations. We assume a polychromatic incident field with a planar wavefront and a CSD of the Gaussian form

$$W_0(x_1, x_2; \omega) = S_0(\omega) \exp\left[-\frac{(x_1 - x_2)^2}{2\sigma^2} \right] \tag{61}$$

where σ is assumed to be frequency independent for simplicity, although this is an unlikely scenario in practise. Using Eq. (24), normalizing according to Eq. (21), and assuming that the pinholes are located at $x_j = \pm a/2$, the true time-domain spatial DOC is found to be

$$\gamma_0(-a/2, a/2; 0) = \exp\left(-\frac{a^2}{2\sigma^2} \right). \tag{62}$$

On the other hand, the spectral interference pattern takes the form

$$S(X; \omega) = 2 |K_0|^2 S_0(\omega) \left(\frac{\omega}{\omega_0} \right)^2 \times \left[1 + \exp\left(-\frac{a^2}{2\sigma^2} \right) \cos\left(a \frac{\omega}{c} \frac{X}{L} \right) \right]. \tag{63}$$

In our illustrations we assume a blackbody spectrum

$$S_0(\omega) = S_0 \frac{(\omega/\omega_0)^3}{\exp(b\omega/\omega_0) - 1}. \tag{64}$$

Here S_0 is a constant, $b = \hbar\omega_0/k_{\mathrm{B}}T$, where $\hbar$ and k_{B} are the reduced Planck constant and the Boltzmann constant, respectively, and T denotes temperature. We set $T = 5780$ K, which is the effective temperature of the Sun [74]. According to Wien's displacement law, this gives the maximum of Planck's law in wavelength scale at $\lambda_{\max} \approx 500$ nm, which corresponds to a reference frequency $\omega_0 = 2\pi c/\lambda_{\max} = 3.77 \times 10^{15}$ Hz.

Figure 6 shows a set of simulation results obtained with the present model. In 6(a) we show the dependence of the spectral interference pattern on X/L in wavelength scale when $a = \sigma = 500\lambda_0$, in which case the fringe contrast is reasonably high across the spectrum. Here the lower limit of the shown wavelength range corresponds roughly to the transmission of typical optical glasses, while the upper limit represents the bandgap wavelength $\lambda = 1.1$ μm of silicon based photodetectors.

The frequency-integrated interference pattern, obtained from Eq. (25), is shown as a function of X/L by the blue curve in Fig. 6(b), whereas the red and green curves represent the top and bottom envelopes of the pattern. Obviously, the standard definition of the visibility of the time-domain interference pattern,

$$V(\mathbf{R}) = \frac{I_{\max} - I_{\min}}{I_{\max} + I_{\min}}, \tag{65}$$

becomes meaningless for the broadband field considered here since the maxima and minima depend strongly on X near the equal-path position $X = 0$. The problem persist even if we assume fully coherent illumination ($\sigma \to \infty$), but it decreases when the bandwidth is reduced towards the quasimonochromatic case. This is illustrated in Fig. 6(c). Here we assume that a bandpass filter with flat transmission over a wavelength range $\lambda_{\max} - \Delta\lambda_0/2 < \lambda < \lambda_{\max} + \Delta\lambda_0/2$ is placed in front of the pinholes and show the top envelopes of the interference pattern when $\Delta\lambda_0 = 100$ nm (red), $\Delta\lambda_0 = 20$ nm (green), and $\Delta\lambda_0 = 4$ nm (blue). With the 4 nm bandwidth the definition in Eq. (65) is applicable for determination of visibility (and therefore the time-domain degree of spatial coherence, which has a true value $\mathrm{e}^{-1/2} \approx 0.6065$ in this case) by using several central fringes between the vertical dashed lines. At 20 nm bandwidth the time-domain DOC can still be determined quite well in this way. Roughly speaking, we may conclude that Young's interferometer can be used for time-domain spatial coherence measurement for bandwidths up to a few tens of nanometers.

It is possible to reduce the above-discussed problems of the traditional Young's interferometer by making the setup achromatic. This can be accomplished by means of achromatic Fourier (or Fresnel) transform (AFT) systems between the two screens in Young's interferometer. Such systems can be constructed using purely refractive components [75–77] or hybrid systems involving both diffractive and refractive components [78, 79]. Ideally, AFT systems eliminate the linear frequency dependence in the exponential term in Eq. (25), thus allowing accurate measurement of time-domain spatial coherence at least if we can approximate $(\omega/\omega_0)^2 \approx 1$ in the frequency integrals. In fact, the effect of this factor can be simulated and the true coherence function can then be retrieved by calibration of the experimental results.

Real AFT systems always have some residual chromatic aberrations, which causes the interference fringes to be only approximately independent of ω. This is because AFTs equalize the transverse scale at only two wavelengths. The use of apochromatic Fourier transform systems would reduce these residual effects significantly, at the expense of having a more complicated system, but we are not aware of any such designs. There seem to be no detailed studies on the performance of AFTs in spatial coherence measurements, but according to experimental evidence [79] such systems perform adequately at least for spectra consisting of red, green, and blue components.

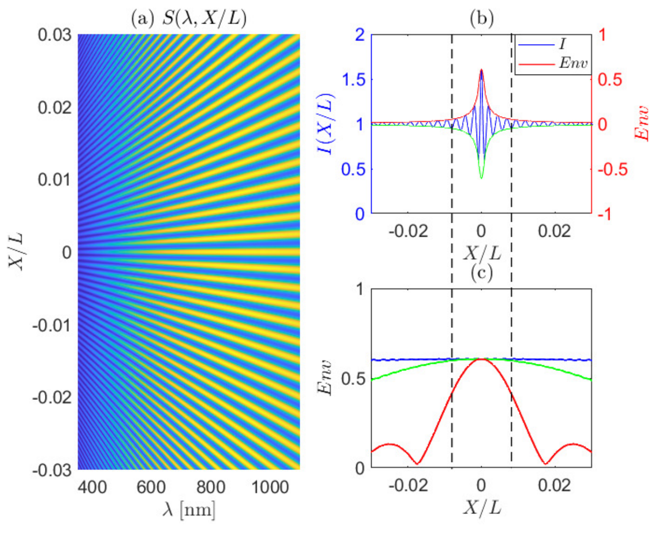

Fig. 6. (a) The spectral interference pattern in Young's experiment for a pair of pinholes at $x_j = \pm a/2$ separated by a distance $a = \sigma$. (b) The blue line is the frequency-integrated interference pattern measured by Young's interferometer when the entire wavelength range in (a) is considered, while the red and green lines represent its envelope. (c) The top envelope when a finite wavelength band is extracted by a band pass filter with flat response over a wavelength band of 4 nm (blue), 20 nm (green), and 100 nm (red).

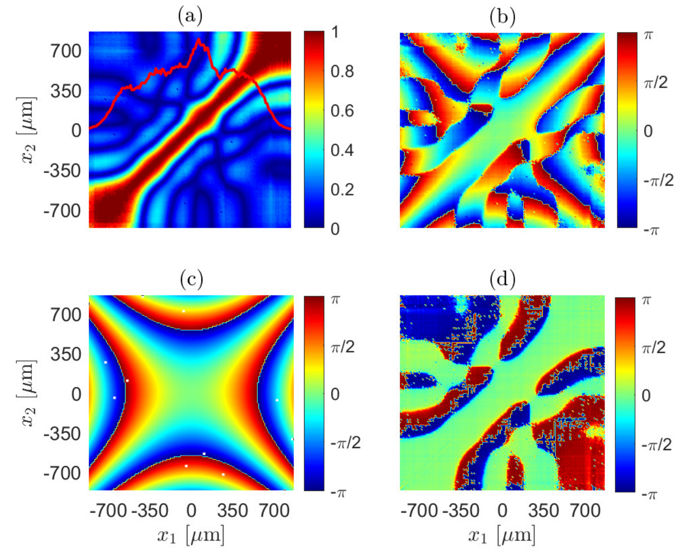

Fig. 7. Illustration of (a) the absolute value and (b) the phase of the complex degree of coherence $\gamma(x_1, x_2; 0)$ of a typical multimode HeNe laser beam, measured by DMD, in the (x_1, x_2) coordinate system. The red line in (a) shows the transverse intensity profile at the beam center. Subfigure (c) shows the best-fitting spherical phase front and (d) represents the phase $\delta_0(x_1, x_2; 0)$ obtained after extraction of the spherical part. Here we have 161×161 data points.

Considering practical measurement issues, before spatial light modulators (SLMs) became readily available, controlling the positions of the pinholes required mechanical movement of, e.g., two cross-shaped binary-amplitude transparency masks relative to each other [52]. This used to be a slow process, limiting the measurements primarily to some fixed (x_1, y_1) and scanning (x_2, y_2) in one or two dimensions. However, SLMs with binary-amplitude transmission or reflectance allow free choice of the positions of both pinholes and substantially faster data acquisition. The devices operate at refreshment rates on the order of 50–60 Hz. It is possible to drive SLMs faster, but this comes at the expense of reduced resolution. Let us assume that the source is bright enough, and three frames are taken (with 75 ms exposure time) at each position to measure patterns with either only one or both pinholes open. The time required to capture and store the data at a fixed pair of points, and finally refresh the pinhole positions to the next pair of points, is on the order of ~ 250 ms. Hence the measurement of, say, 128×128 point-position combinations takes $\sim$1 hour at refresh rate of 60 Hz. This rate applies to typical digital micromirror devices (DMDs), which we favor for implementing Young's interferometer mainly because they offer high pinhole/background contrast [80]. However, the acquisition times are of the same order of magnitude for other SLMs as well. We may conclude at this point that measurements for a limited number of samples of $\mathbf{r}_1$ at a reasonable resolution along $\mathbf{r}_2$ is feasible, but the measurement of full 4D data with $M = N = P = R$ at even decent resolution is out of the question.

Obviously, since the incident field at the input plane A of the setup is sampled by small pinholes (formed with $M \times N$ SLM pixels), the light efficiency of Young's interferometer cannot be very high. To obtain an order-of-magnitude estimate we assume that the average power of the field on the illuminated area in plane A is $\bar{P}_\mathrm{A}$. Then the average power level at the detector plane is $\bar{P}_\mathrm{B} \sim 2\bar{P}_\mathrm{A} A_m MN/L^2$, where A_m is the area of a single SLM pixel (or DMD mirror), and L is the distance between planes A and B. Therefore, the light efficiency of the device is roughly $\bar{P}_\mathrm{B}/\bar{P}_\mathrm{A} \sim 2A_m MN/L^2$

In our experience, a sufficient SNR for coherence measurements is $\sim$ 100. With standard CCD/CMOS detectors operating at room temperature (with a quantum efficiency of $\sim 70\%$), this translates to incident power on the detection area greater than $\bar{P}_\mathrm{B} \sim 1\ \mathrm{nW/cm^2}$. Thus, with $M \times N \sim 100 \times 100$, the power at plane A should be at least on the level $\bar{P}_\mathrm{A} = L^2/A_m \times 10\ \mu\mathrm{W/cm^2}$. The factor L^2/A_m depends on the employed system and it is often on the order of ~ 100. Moreover, if we add spectral resolution, the power incident on plane A has to be $\sim Q$ times larger to resolve Q spectral samples.

F. Measurement examples

In the first example we consider a beam emitted from a typical HeNe laser cavity that supports several HG modes in both x and y directions. Since the beam is quasimonochromatic, the time-domain coherence properties can be retrieved directly from the measurements, performed here with a DMD device. The measurements were done by illuminating the DMD directly by a beam with an intensity distribution that essentially fits within an area $1.728 \times 1.728\ \mathrm{mm}^2$ considered in Fig. 7. Figures 7(a) and 7(b) show the measured distributions of $|\gamma(x_1, x_2; 0)|$ and $\delta(x_1, x_2; 0)$, wrapped in the interval $[-\pi, \pi]$, respectively. The wavefront of the beam incident on the DMD is not perfectly planar but contains a deterministic spherical phase of the form of Eq. (46), introduced by propagation. This phase, shown in 7(c), is determined by a numerical best-fitting procedure. Once extracted from the phase shown in 7(b), we obtain the random part $\delta 0(x_1, x_2; 0)$ of the phase, which is illustrated in 7(d).

The second example demonstrates the measurement of the spectral coherence Stokes parameters of a light beam with a spectrally resolved Young's interferometer based on a DMD device, a grating spectrometer, and a set of circular polarizers [81]. The source is a superluminescent diode emitting linearly polarized, spatially partially coherent light at a center wavelength of 670 nm with spectral full width at half-maximum of 7.5 nm. The spectral and spatial polarization structure of the beam is modulated using a quartz-wedge depolarizer. Figures 8(a)–(d) show the spatial distributions of the normalized coherence Stokes parameters $\mu_n(x_1, x_2, \omega)$, $n \in (0, \ldots, 3)$, at a wavelength of 659.4 nm. The figures illustrate a complex polarization-coherence structure that may exists at a single wavelength. Although not shown here, it was found in [81] that the polarization and electromagnetic coherence properties may vary with wavelength on a scale of less than one nanometer. Despite the rich spatio-spectral structure of the coherence Stokes parameters, the degree of coherence shown in Fig. 8(e) is rather smooth and coincides with that of the source since the degree is unaffected by the point-wise unitary transformations (corresponding to waveplates) produced by the wedge depolarizer.

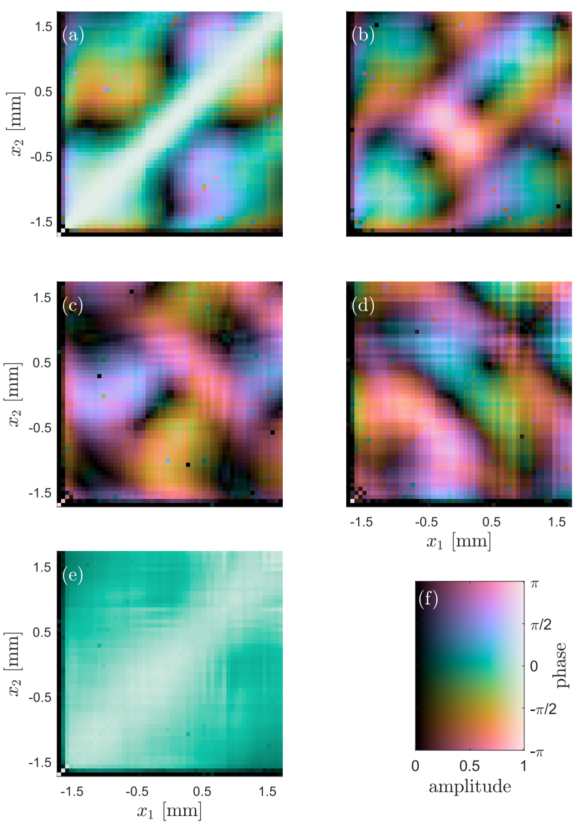

Fig. 8. Illustration of the measured normalized coherence Stokes parameters (a) $\mu_0(x_1, x_2, \omega)$, (b) $\mu_1(x_1, x_2, \omega)$, (c) $\mu_2(x_1, x_2, \omega)$, (d) $\mu_3(x_1, x_2, \omega)$, and (e) the degree of coherence $\mu(x_1, x_2, \omega)$. The plots are for $\lambda = 659.4$ nm and the number of data points is 56×56. The colors contain information on both the amplitude and phase of the complex-valued quantities as shown in the two-axis colormap in (f). Adapted from Ref. [81].

5. WAVEFRONT FOLDING AND SHEARING INTERFEROMETERS

The practical shortcomings of Young's two-beam experiment, regarding measurement speed in particular, can be largely avoided by techniques that measure spatial coherence for a (large) set of points in parallel. In this section we consider a class of techniques that do this by interfering the wavefront to be measured with its laterally folded or sheared replica. Since these techniques are based on reflections of the original beam rather than diffraction by pinholes, they are also highly light-efficient.

A. Operation principles and implementations

Figure 9 illustrates the operating principles of wavefront folding interferometer (WFI) and wavefront shearing interferometer (WSI), for coherence measurements of a beam-like incident field along one spatial dimension (here the x direction). The detector D is an array sensor (such as CCD or CMOS) if we wish to measure white-light interference, or a spectrometer (providing spectral resolution in the y direction) if we wish to measure spectral interference. In both cases the losses are mainly due to the beam splitters if the field fits within the aperture of the device.

Wavefront folding interferometers have been used for coherence measurements for over half a century [63, 82–84]. The original implementation employed 2D folding WFIs, with the plane mirror in Fig. 9(a) replaced by a retroreflecor that folds the incident field also in the y direction. However, these devices were aligned such that the corners of both retroreflectors were placed on the optical axis ($s = 0$ in Fig. 9), thus providing coherence information only between two axially symmetric points as we will shortly see. In Fig. 9(a) we consider a 1D folding version with an arbitrary shear s, which allows the determination of spatial coherence between any two points x_1 and x_2.

Figure 9(a) also illustrates ray propagation through the two arms of the WFI (horizontal arm 1 with the retroreflector R and vertical arm 2 with the plane mirror M). The (solid red) ray that originates from an arbitrary point x_1 ends up at point $X = x_1$ when traveling through arm 2. On the other hand, we see that the (solid green) ray originating from point $x_2 = -x_1 + 2s$ also ends up at the point $X = x_1$ in the output plane when traveling through arm 1 (the alternating green-red line indicates ray paths in the region where they overlap). This leads to interference between the fields located at positions x_1 and x_2 in the input plane. An array detector D therefore measures interference between any x_1 and the corresponding x_2 in parallel. Setting, in particular, $s = 0$ gives $x_2 = -x_1$. When the shift s is tuned, we can measure interference between arbitrary points x_1 and x_2.

A longitudinal shift Δz is used in practical devices to enable control of the optical path length difference between arms 1 and 2; we can take $\Delta z = 0$ to represent the equal-path configuration. Considering the spectral representation of the incident field and denoting this by $E_0(x;\omega)$, the interference in the X direction at the detector plane can now be expressed as

$$E(X;\omega) = \frac{1}{2}\left\{E_0(x;\omega) + E_0(2s - x;\omega)\exp\left[i\Delta\phi(\omega)\right]\right\}. \quad \mathbf{(66)}$$

Here the factor $1/2$ arises from beam splitter loss and we have written $\Delta\phi(\omega) = 2(\omega/c)\Delta z$ for brevity. Proceeding in analogy with Sect. 4A, the spectral interference pattern at the output plane takes the form

$$S(X;\omega) = \frac{1}{4}\left[S_0(x;\omega) + S_0(2s - x;\omega)\right] + \frac{1}{2}\Big\{\sqrt{S_0(x;\omega)S_0(2s-x;\omega)}\,|\mu_0(x,2s-x;\omega)| \times \cos\left[\alpha_0(x,2s-x;\omega) + \Delta\phi(\omega)\right]\Big\}. \quad (67)$$

Interference fringes are seen when $\Delta\phi(\omega)$ is varied over a small region (a few wavelengths) from the equal-path position. Alternatively, we can see fringes in the lateral direction by tilting M in either x or y direction, or by tilting R in the y direction. We obtain the absolute value of the complex degree of spatial coherence at point X by measuring the fringe visibility, which now reads as

$$V(X;\omega) = \frac{2\sqrt{S_0(x;\omega)S_0(2s-x;\omega)}}{S_0(x;\omega) + S_0(2s-x;\omega)}\,|\mu_0(x,2s-x;\omega)|. \quad (68)$$

On the other hand, the phase $\alpha_0(x, 2s - x;\omega)$ can be determined from fringe positions.

Lateral shearing interferometry has long been one of the standard methods for optical testing (see Chapt. 4 in Ref. [85]), where its performance is limited by coherence of the wavefront to be characterized. From the point of view of spatial coherence measurements, this limitation becomes an advantage if we employ reflection-type setups as illustrated in Fig. 9(b). An essentially similar arrangement was used by Efimov [86, 87] specifically to characterize spatial coherence of light emerging from multimode fibers. However, the technique is generally applicable and shares the advantages of the WFI.

The only difference between the WFI and the WSI implementation shown in Fig. 9 is that the plane mirror in the former is replaced with a retroreflector also in the vertical arm. As seen by following the red ray, this retroreflector maps any point x_1 in the input plane to point $X = -x_1$ at the output plane. The green ray originating from point $x_2 = x_1 + 2s$ is also seen to hit the output plane at $X = -x_1$ when traveling though arm 1. As a result, we obtain interference of the folded replica of the input field with its folded *and* sheared (by an amount $2s$) replica. Mathematically, the field at point X in the output plane of the WSI takes the form

$$E(X;\omega) = \frac{1}{2}\left\{E_0(-x;\omega) + E_0(2s-x;\omega)\exp\left[i\Delta\phi(\omega)\right]\right\}. \quad (69)$$

If the shift $s = 0$, the WSI thus produces just a reversed replica of the input field. The spectral interference pattern produced by the WSI is given by

$$S(X;\omega) = \frac{1}{4}\left[S_0(-x;\omega) + S_0(2s - x;\omega)\right] + \frac{1}{2}\Big\{\sqrt{S_0(-x;\omega)S_0(2s-x;\omega)}\,|\mu_0(-x,2s-x;\omega)| \times \cos\left[\alpha_0(-x,2s-x;\omega) + \Delta\phi(\omega)\right]\Big\}. \quad (70)$$

Interference fringes can again be observed by scanning Δz over a small range. Spatial fringes can be seen, but only in the y direction, by tilting either retroreflector in this direction.

One practical problem with the retroreflector-based implementations of both the WFI and the WSI shown in Fig. 9 is caused by the corners of the retroreflectors. These corners produce substantial (far larger than one might expect) diffraction effects at the output plane even if the device is compact (our laboratory implementations measure around $10 \times 10 \times 10$ cm).

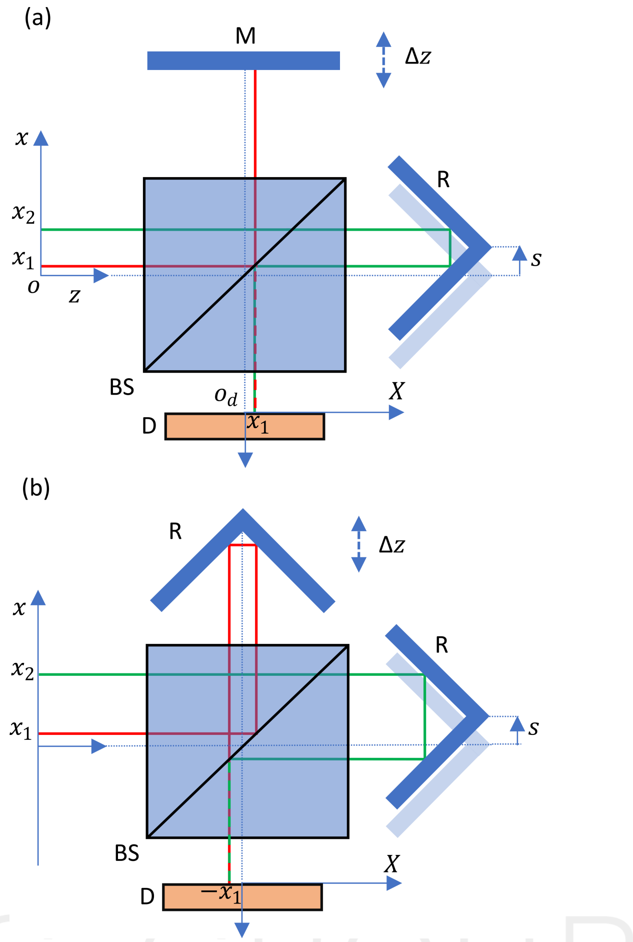

Fig. 9. Schematic cross-sectional views of (a) a 1D folding WFI and (b) a 1D shearing WSI. BS: non-polarizing beam splitter. R: L-shaped mirror or a 90° prism (retroreflector). M: plane mirror. D: detector. Here s represents a lateral shift in positive x direction and Δz a shift from the equal-path position.

These effects essentially forbid coherence measurements when one of the input points is close to the corner. One can reduce (but not completely eliminate) these problems by imaging the input plane first onto the plane of the corners, and then the latter plane onto the output plane. However, this leads to a substantial increase in the physical size of the entire setup, yet still the corners remain visible at the output plane. If the conjugate distances of the imaging system are chosen such that the field at this plane is spatially large compared to the width of the disturbance caused by the corners, the effect is rather negligible for coherence measurements purposes.

The corner effects can be eliminated completely by using implementations based on planar mirrors only, as illustrated in Fig. 10. The system in Fig. 10(a) was introduced rather recently [88, 89], while that in Fig. 10(b) is new. It may be worth noting at this point that especially the WFI has applications other than spatial coherence measurements. For instance, it can be used to generate novel special types of fields that do not obey the Schell model. It was shown already in 1988 [90] that a WFI is capable of generating so-called specular CSDs, while the method was demonstrated much more recently [91]. However, in Ref. [91] corner diffraction prevented studies of propagation of specular beams, a problem that was solved only after the

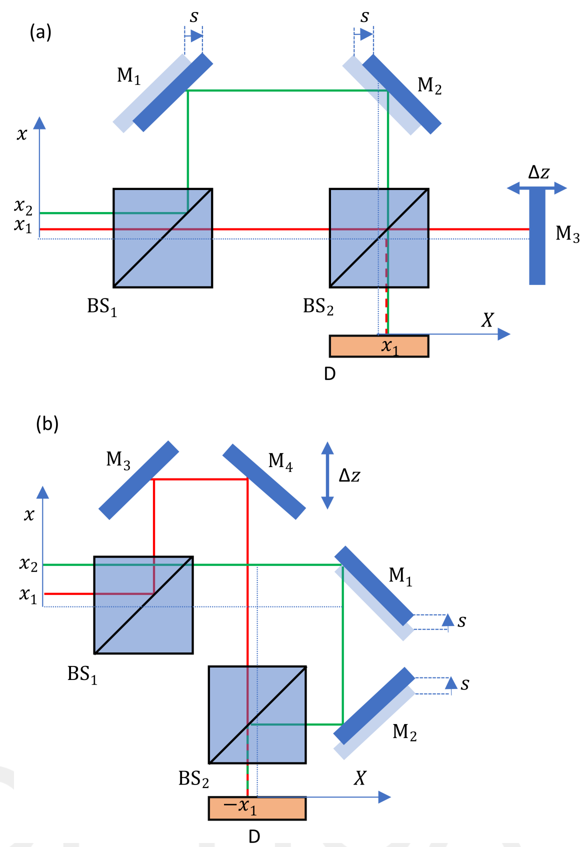

Fig. 10. Same as Fig. 9, but for mirror-based implementations of (a) the WFI and (b) the WSI. M_1–M_4 are plane mirrors, while BS_1 and BS_2 are beam splitters.

mirror-based WFI became available [92]. Another advantage, relevant for the WSI, is that we may introduce tilt also in the x direction, which is necessary if the y direction is reserved for resolving the spectrum. Apart from eliminating the corner effects, the mirror based WFI and WSI setups have other, perhaps more relevant advantages over retroreflector-based implementations. The latter may modulate the polarization state of the incident field rather strongly. For instance, if we use retroreflecting prisms with a refractive index of ~ 1.5 and the incident light is circularly polarized, the visibility of the resulting interference fringes is low even if the light is completely coherent and polarized [88]. Such effects are reduced dramatically in the mirror based approach, making them negligible for most purposes. Thus, both the WFI and WSI setups are suitable for measuring fields with nontrivial polarization states. When combined with suitable polarization modulation devices, they also allow for the measurement of the coherence Stokes parameters in a way analogous to Young's DMD setup discussed in Sect. 4F [81].

The difference between the WFI and the WSI is the placement of the prisms and the number of required mirrors. Here it needs to be noted that the WFI implementation in Fig. 10(a) is a special case, where one beam meets a beam splitter two times, while the other beam meets a beam splitter three times. This increases losses, and needs to be taken into account in the theoretical formulation (see Ref. [88]). In the WFI three mirrors are needed, corresponding to one retroreflector and one plane mirror in Fig. 9(a), whereas four mirrors are required for the WSI, corresponding to two retroreflectors in Fig. 9(b). In both WFI and WSI systems, the lateral shift, s, is realized by moving mirrors M_1 and M_2 together. As also indicated in Fig. 10, the Δz scan is accomplished by moving M_3 in the WFI, while mirrors M_3 and M_4 are moved to achieve the same purpose in the WSI. By following the red and greens rays one can readily see that Eq. (66) holds for the mirror-based WFI and Eq. (69) holds for the mirror-based WSI.

In general we need configurations that fold or shift the incident field in two orthogonal directions (x and y). Mirror-based configurations of these devices, essentially as we have constructed them, are illustrated in three dimensions in Fig. 11. Before explaining these in more detail, we note that the mathematical formulation for both the WFI and the WSI are simple extensions of the 1D formulations presented above, assuming shifts s_x and s_y, and writing the expressions in terms of detector coordinates X and Y. Doing this, we have

$$E(X,Y;\omega) = \frac{1}{2}\{E_0(x,y;\omega) + E_0(2s_x - x, 2s_y - y;\omega)\exp[i\Delta\phi(\omega)]\}, \quad \textbf{(71)}$$

for the WFI and

$$E(X,Y;\omega) = \frac{1}{2}\{E_0(-x,-y;\omega) + E_0(2s_x - x, 2s_y - y;\omega)\exp[i\Delta\phi(\omega)]\}, \quad \textbf{(72)}$$

for the WSI. The spectral interference patterns are corresponding generalizations of Eqs. (67) and (70).

Figures 11(a) and 11(b) also illustrate rays propagating through perfectly aligned (no lateral shifts) mirror-based 2D WFI and WSI systems, respectively. In both cases, the incident beam arrives at the first beam splitter, BS_1, and splits into two identical copies. One of the replicas travels through arm 1, which has four mirrors M_1–M_4, while the other one goes through arm 2 with mirrors M_5 and M_6. At the second beam splitter, BS_2, the two replicas are superimposed and produce outputs 1 and 2. Here (x, y) represents the ray coordinates at the input plane, whereas (X, Y) are associated with the detector plane coordinates at output 2.

The two systems presented in Figs. 11(a) and 11(b) have some basic operational differences analogous to their 1D counterparts. In the case of WFI the incident beam travels through arm 1 and flips along the X-direction, whereas a beam that passes through arm 2 flips along the Y-direction. If the mirrors M_2 and M_3 are jointly shifted by an amount s_x, the principal ray shifts towards positive X-direction as shown in 10(a). Correspondingly, if M_5 and M_6 are shifted together by an amount s_y, the principal ray shifts the same amount in the positive Y-direction. In the case of the WSI neither of the wavefronts is flipped at output 2, whereas they are both flipped at output 1. Jointly shearing M_2 and M_3 by an amount s_x, or M_5 and M_6 by s_y, shifts the principal ray towards negative X and Y, respectively, in analogy with the 1D WSI setup in 10(b). Moreover, for WFI, the shifts (s_x, s_y) can also be introduced by scanning the whole setup with respect to the input beam, see, e.g., the description in Ref. [89].

In the space-time domain the output-plane fields of the WFI and WSI are obtained by applying Eq. (19). Using also Eqs. (1) and (11) we obtain (up to a common phase factor) the result

$$E(X;t) = \frac{1}{2}[E_0(x;t-\tau_1) + E_0(2s - x;t-\tau_2)] \quad \textbf{(73)}$$

for the WFI and

$$E(X;t) = \frac{1}{2}[E_0(-x;t-\tau_2) + E_0(2s - x;t-\tau_2)] \quad \textbf{(74)}$$

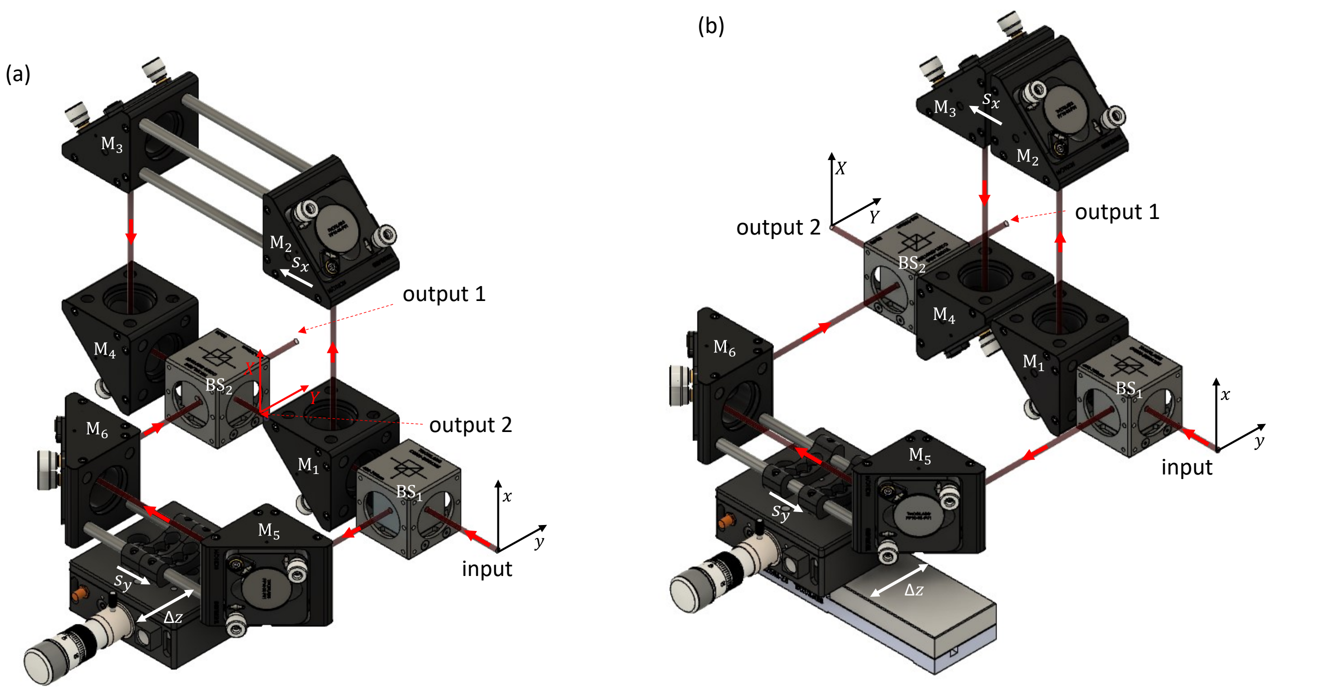

Fig. 11. 3D views of (a) a mirror-based 2D folding WFI and (b) WSI. M_1–M_6 are plane mirrors, while BS_1 and BS_2 are beam splitters. Coordinates (x, y) belong to the source-plane and (X, Y) represents the detector-plane coordinates at output port 2. The delay Δz between the two arms can be controlled over an arbitrary range using a mechanical translation stage, which can be fine-tuned at sub-wavelength precision by a piezoelectric device.

for the WSI. In these expressions we have defined $\tau_1 = \phi(x_1;\omega_0)/\omega_0$ and $\tau_2 = \phi(x_2;\omega_0)/\omega_0 + 2\Delta z/c$. Hence, writing $\Delta\tau = \tau_2 - \tau_1$, the time-domain interference patterns are

$$I(X;\Delta\tau) = \frac{1}{4}\left[I_0(x) + I_0(2s-x)\right] + \frac{1}{2}\Big\{\sqrt{I_0(x)I_0(2s-x)}\,|\gamma_0(x,2s-x;\Delta\tau)| \times \cos\left[\delta_0(x,2s-x;\Delta\tau) + \Delta\tau\right]\Big\} \tag{75}$$

and

$$I(X;\Delta\tau) = \frac{1}{4}\left[I_0(-x) + I_0(2s-x)\right] + \frac{1}{2}\Big\{\sqrt{I_0(-x)I_0(2s-x)}\,|\gamma_0(-x,2s-x;\Delta\tau)| \times \cos\left[\delta_0(-x,2s-x;\Delta\tau) + \Delta\tau\right]\Big\}, \tag{76}$$

respectively. Corresponding expressions can be written for the 2D configurations as well. Obviously both devices also facilitate spatio-temporal coherence measurements if we vary the delay $\Delta\tau$ over a region larger than the coherence time of the incident field. This is analogous to measuring (only) temporal coherence with Michelson's interferometer.

B. Experimental aspects and performance

As emphasized in Sect. 3B, the dimensionality of the data affects the required storage space, though this is not usually a critical issue. More importantly, it affects data acquisition speed in Young-type setups. The WFI and WSI offer dramatic improvements in acquisition speed since measurements can be done in parallel over the area where the beams overlap. That is, each measurement in both WFI and WSI yields a slice of the spatial correlation function, albeit in different directions. The WFI measures the correlations along the anti-diagonal of the correlation function, while the WSI does the same along the diagonal. If we are measuring along one transverse coordinate and each measurement comprises of a range of points, we only need to scan the beams across each other once to obtain the 2D coherence function. In other words, the total measurement time of 2D coherence functions with these methods scales linearly with the number of scanned points, whereas the measurement time for a DMD-based Young's interferometer scales quadratically. As a rule of thumb, the acquisition time for a $2m$-dimensional correlation function scales to the power of $2m$ with a Young's experiment, while it scales to the power of m for the WFI and WSI.

The main limiting factor for acquisition time is the mechanical movement of shutters and stages. The total time of acquiring one 2D slice of a 4D correlation function takes ~ 1 s, which makes it feasible to measure correlation functions with a resolution of $M = N \approx 1000$ in the transverse direction, and $P = R \approx 100$ in the scanning direction within hours. This is usually sufficient for further analysis. The setups in Fig. 11 are robust, thus allowing measurement times up to several days. Further, since they have two alternative outputs, one of them is available for monitoring of possible instabilities.

Regarding the required power level $\bar{P}_A$, we note that if the field to be measured fits within the aperture of the instrument, then $\bar{P}_B \approx 0.25\bar{P}_A$. Hence, we have $\bar{P}_A \approx 4Q\bar{P}_B$, where Q is again the number of spectral samples. Effectively, therefore, if the intensity profile across the beam can be measured by the detector, the spatial coherence is measurable as well. The ability of the WFI to characterize weak fields has recently been demonstrated by coherence measurements for plasmonic lattice lasers

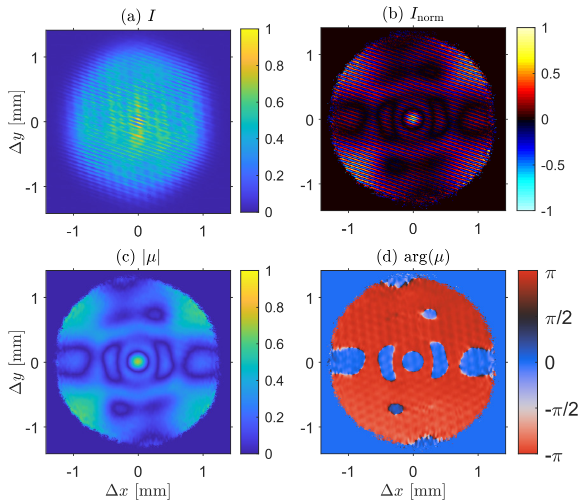

Fig. 12. Illustration of the interference fringes and extraction of $\mu(\Delta x, \Delta y)$ of typical beam from a multi-mode HeNe laser, measured with WFI. (a) the captured interference fringes, (b) the normalized interference pattern, (c) absolute value and (d) phase of the complex degree of spatial coherence in $(\Delta x, \Delta y)$ coordinate system, at $\Delta\tau = 0$. See Visualization 2 for animation of the full scan. The figure is produced using the data from Ref. [89].

operating even below the lasing threshold [93].

C. Measurement examples

The cross-spectral density function $W(x_1, y_1, x_2, y_2; \Delta z)$ as well as the complex degree of spatial coherence $\mu(x_1, y_1, x_2, y_2; \Delta z)$ can both be represented in the average and difference coordinate system as $W(\bar{x}, \Delta x, \bar{y}, \Delta y; \Delta z)$ and $\mu(\bar{x}, \Delta x, \bar{y}, \Delta y; \Delta z)$, respectively. This corresponds to a rotation of 45 degree rotation, with the average coordinates defined as $\bar{x} = (x_2 + x_1)/2$ and $\bar{y} = (y_2 + y_1)/2$, and the difference coordinates as $\Delta x = x_2 - x_1$ and $\Delta y = y_2 - y_1$. This is actually the native coordinate system for the WFI.

Two measurement examples are presented. In Fig. 12 the source is a multimode HeNe laser (Lasos LGK 7621 MM), while in Fig. 13 we consider a multimode broad area laser diode (BALD, Opnext HL6388MG) operating at 280 mA. In both cases we measured the full 4D correlation function correlation function by 2D WI, of which only cross sections can be visualized in two dimensions.

Starting from the HeNe case, an interference pattern recorded directly by a CMOS camera, with the WFI set at axial average coordinates $(\bar{x}, \bar{y}) = (0, 0)$, is shown in Fig. 12(a). In Fig. 12(b) we show the interference pattern normalized with the use of single-beam images (i.e., beams passing through only one arm) [88, 89]. The absolute value and phase of the complex degree of coherence is then extracted using standard Fourier signal processing techniques [88, 89]. The results are presented in Figs. 12(c) and (d), respectively. In this example coherence is modulated along both (Δx and Δy) axis, which is due to several HG modes being excited during the lasing operation. Thus the field is not of the Schell-model form and 4D measurements are needed for its accurate characterization. Visualization 2 shows the full measurement with scan over both transverse axes.

Results of corresponding measurement for BALD are presented in Fig. 13. The BALD is highly spatially coherent along the horizontal axis, whereas it is spatially partially coherent along the vertical direction. This is due to the anisotropic cavity dimensions (narrow horizontally and wide vertically) which allows for multimode action along the vertical axis but not along the horizontal axis. This leads to the absolute value of the DOC concentrating near the vertical axis, but again the field is not of the Schell-model form.

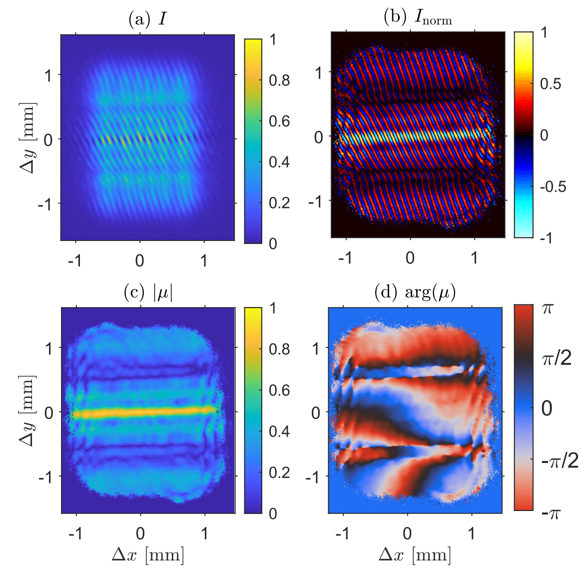

Fig. 13. Same as Fig. 12 except the source is BALD. This figure is produced from the data in Ref. [89].

In both the cases (Figs. 12 and 13) we get 1024×1280 data points (limited by the total number of camera pixels) in $(\Delta x, \Delta y)$ coordinates, and a single measurement takes $\approx$ 2-3 seconds. Similar measurement with a DMD-based Young's interferometer would take $\sim$ 12 hours.

6. OTHER TECHNIQUES

The measurement of spatial coherence can be done with a diverse set of techniques, each with their unique advantages and limitations. Below is a non-exhaustive list of measurement schemes introduced over the years, with a short discussion on their properties.

A. Reversed-wavefront interferometer

The traditional Young's interferometer can be modified in several ways to improve its applicability. For example, the reversed-wavefront method is an extension which modifies the input of Young's interferometer [94]. To be more specific, the incident beam is split into two in such a manner that one of the copies is flipped (or reversed). Afterwards, the two copies are fed into two different pinholes and the resulting interference pattern is recorded at the observation plane. A possible implementation of this scheme is shown in Fig. 14 below.

The field that is incident on the two pinholes is of the same form as in the WFI, that is

$$E(X;\omega) = \frac{1}{2}\left\{E_0(x;\omega) + E_0(d-x;\omega)\exp\left[i\Delta\phi(\omega)\right]\right\}, \quad (77)$$

where d is the distance between the copies. The reversed-wavefront interferometer therefore measures a similar interference pattern as the WFI, although the pattern is sampled at the

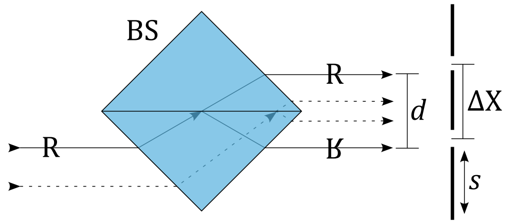

Fig. 14. The original reversal scheme in Ref. [94]. The light is incident on a beam splitter BS, which produces two copies of the input beam. The lower beam is reversed due to the reflection inside the beam splitter cube as illustrated with the letter R, while the dashed line shows an alternative route for the beam. The measured interference pattern depends on the distance d between the copies, the shear s, and the distance ΔX between the pinholes.

positions of the pinholes instead of overlapping all possible coordinate pairs along the measurement direction. The sampling positions depend on d, as well as the relative position of the pinholes. The distance d can be varied by moving the input position at the beam splitter (see the dashed line in Fig. 14), while the pinholes can be sheared by an amount s over the two copies.

The advantage in the reversed-wavefront method is that it is able to measure all combinations of spatial points with the use of a single (static) mask. This removes the need for SLMs or DMDs that are able to produce all possible coordinate combinations. Instead, the scanning is performed simply by scanning the beam across the device input. However, this comes at the price of low light efficiency, which is already a notable problem in the usual Young's interferometer.

B. Multiple apertures

Another method that can be thought of as an extension of the traditional Young's interferometer is the multiple apertures method. Just as the name implies, it is a scheme where several pinholes are employed instead of just two [95, 96]. One can choose the number and position of the apertures such that the resultant interference pattern contains coherence information for multiple pairs of points along the wavefront, as depicted in Fig 15. If there are N pinholes in the mask, this corresponds up to $(N-1)!$ pairs of measurement points [95]. In particular, the relative amplitudes of the Fourier spectrum is directly proportional to the correlations between the chosen points as in

$$\tilde{I}(\mathbf{r}) = \Lambda(\mathbf{r}) \otimes \left[\sum_{i=j} I_j \delta(\mathbf{r}) + \sum_{i \neq j} \sqrt{I_i I_j} \Re\{\mu(\mathbf{r}_i, \mathbf{r}_j) \delta(\mathbf{r} - \mathbf{d}_{ij})\} \right], \tag{78}$$

where $\tilde{I}$ is the Fourier transform of the observation plane interference pattern, $\otimes$ denotes a convolution, $\Lambda(\mathbf{r})$ is the autocorrelation function of a single pinhole (assuming all pinholes are identical), and subscripts i, j correspond to the pinholes positioned at $\mathbf{r}_i$ and $\mathbf{r}_j$. Therefore, I_i and I_j correspond to the intensities arising from pinholes i and j, $\mathbf{d}_{ij} = \mathbf{r}_i - \mathbf{r}_j$ is a separation vector, and $\mu(\mathbf{r}_i, \mathbf{r}_j)$ is the complex degree of coherence between $\mathbf{r}_i$ and $\mathbf{r}_j$ of the input field. The modulus of $\mu(\mathbf{r}_i, \mathbf{r}_j)$ can be retrieved with

$$|\mu(\mathbf{r}_i, \mathbf{r}_j)| = \frac{C_{ij}}{\sqrt{I_i I_j}} \frac{S_0}{|C_0|}, \tag{79}$$

where $S_0 = \sum_{i=j} I_j$ is the total intensity through the mask, C_0 is the amplitude of the zeroth peak, and C_{ij} is the amplitude of the peak corresponding to $\mathbf{d}_{ij}$.

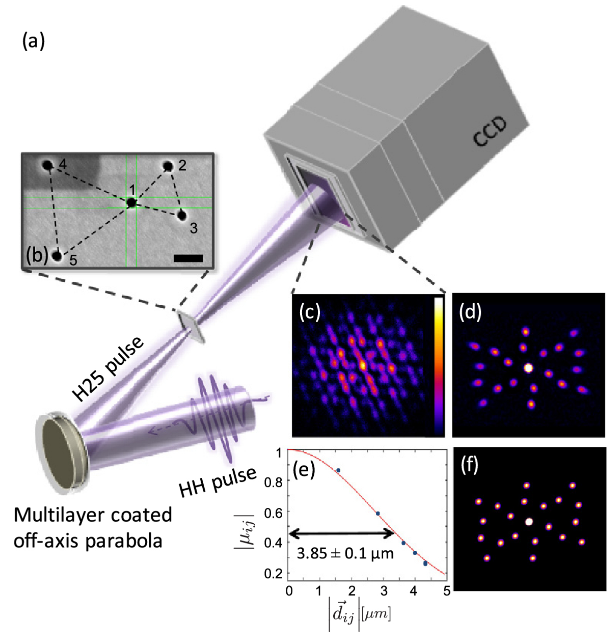

Fig. 15. Multiple aperture experiment with a high harmonic pulse. (a) Depiction of the experimental setup, (b) scanning electron microscope image of a multiple-aperture mask, (c) measured single-shot diffraction pattern, (d) Fourier transform of (c), (e) the retrieved degree of spatial coherence, and (f) the computed autocorrelation of the mask. The color scale of (c) is in arbitrary units and is common for (c), (d), and (f). Reprinted with permission from Ref. [97] © The Optical Society.

This method is particularly useful for the measurement of exotic light sources, such as X-ray FEL and synchrotron radiation. In fact, this technique was recently demonstrated for characterizing X-rays from high harmonic generation [97]. The main reason why the multiple-aperture method is suitable for these sources is high energy of the emitted pulses, which tends to destroy any measurement device, including two-pinhole masks. That is, each time a single pulse has been measured, the mask needs to be moved to a 'fresh' set of pinholes, because the original pinholes have been destroyed [38]. This introduces additional uncertainty to the measurement, since each pinhole pair needs to be measured multiple times and the positioning is not absolute. Moreover, there are hardly any optical elements available at X-ray wavelengths, and performing WFI or WSI type measurements at those frequencies is challenging.

C. Non-parallel slits

Like the multiple aperture approach demonstrates, one is not forced to use only two pinholes in a Young-type interferometer. In fact, it is also possible to employ different geometries for the apertures themselves to obtain more coherence information in a single measurement. One such approach is the non-parallel slit geometry [98], where the separation of the slits varies as a function of position. Let us consider a mask such as the one in Fig. 16(a), where the slit separation gradually decreases along the positive y-axis, in which case one measures

$$S(X,Y;\omega) = |K_0|^2 (\omega/\omega_0)^2 \{S(x-d(y);\omega) + S(x+d(y);\omega) + 2\sqrt{S(x-d(y);\omega)S(x+d(y);\omega)} \times |\mu_0(x-d(y), x+d(y);\omega)| \cos[\Phi(x,y)]\}, \quad (80)$$

where

$$\Phi(x,y) = \alpha_0(x-d(y), x+d(y);\omega) + (\omega/\omega_0)\phi(x-d(y), x+d(y);\omega_0) \quad (81)$$

is the phase of the correlation function. Simply put, the interference pattern varies along the y-axis. Taking a single slice of the interference pattern at some value of y results in the usual interference pattern from a Young's interferometer.

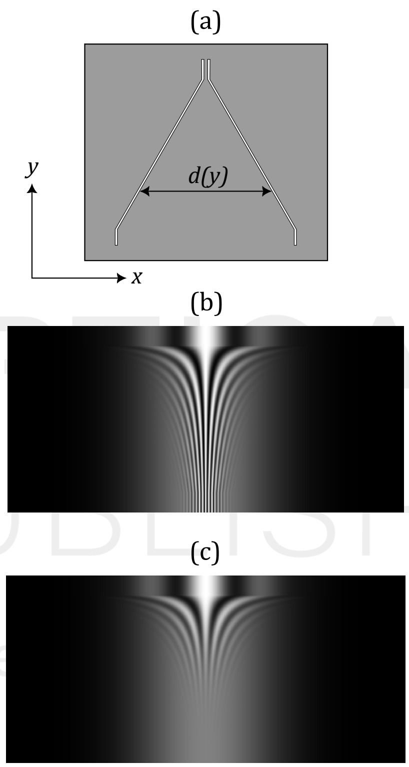

Fig. 16. (a) Non-parallel slit geometry. (b) A simulated interference pattern with completely coherent quasi-monochromatic light. (c) A corresponding pattern with partially coherent quasi-monochromatic light. The interference pattern loses visibility along the x-axis due to path length difference, like in the usual double pinhole setup.

The non-parallel geometry has the obvious advantage that it measures the coherence function with a continuously variable slit separation in a single measurement. The disadvantage of this type of measurements is that the input field needs to be homogeneous and separable to x- and y-dependent components to produce reliable results with just one measurement. These problems can probably be alleviated by performing more measurements, where the beam is laterally displaced at the input side, and by measuring along both transverse axes.

Finally, since this method is able to measure coherence over a continuously variable slit separation in a single measurement (although, with some limitations as discussed above), it is well-suited for measuring high-energy sources like femtosecond X-ray FEL pulses.

D. Scattering particles

It has recently been demonstrated that the two-point spatial coherence properties of light beams can be measured in terms of nanoscattering [99]. Such an arrangement consists of two (dipolar) nanoparticle probes that replace the pinholes of Young's interferometer and the degree of coherence at the particle sites is deduced from the visibility of the intensity fringes generated by the interfering scattered far fields. The nanoprobe and pinhole methods have certain fundamental differences. The particles are of subwavelength size whereas the hole dimensions are several wavelengths, indicating that the probe method implies a superior spatial resolution. In addition, the far fields generated in the two methods are due to aperture diffraction and dipole scattering where in the latter the far-field fringe pattern includes a specific geometric factor.

In the experiments gold-cube nanoparticles with the side length of 130 nm and deposited on a silicon substrate was used. The light source was a multi-mode (low spatial coherence, unpolarized) HeNe laser of wavelength 632.8 nm. The geometry of the experiment is depicted in Fig. 17(a), while (b) shows a scanning electron microscope (SEM) image of a pair of nanoprobes with 3 μm separation. In addition, Fig. 17(c) exemplifies the measured far-field intensity fringes whose visibility specifies the degree of coherence. In analyzing the visibility the dipolar scattering patterns and particle-substrate interactions must be carefully considered [99]. In Fig. 17(d) the colored symbols correspond to the degrees of coherence measured by pairs of nanoparticles with different separations. The solid line shows the degree of coherence obtained by a DMD. The agreement between the nanoprobe and DMD methods is excellent. The nanoscattering method has been extended to the electromagnetic domain where the coherence Stokes parameters are of interest [100, 101].

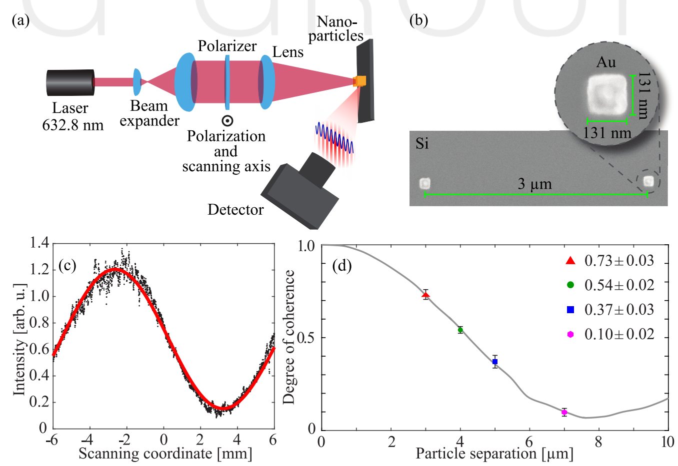

Fig. 17. Two-nanoprobe measurement setup. (a) Illumination, particles, and far-field detection. (b) A SEM image of cubic gold nanoparticles separated by a distance of 3 μm. (c) An example of measured far-field intensity fringes for the particle separation 3 μm. (d) The measured degree of coherence for various particle separations (symbols). The solid blue curve shows the degree obtained by a DMD. Adapted from [99].

E. Sagnac-type interferometers

The well-known Sagnac interferometer can also be modified for use in spatial coherence measurements [102, 103]. Since the wavefront is not folded, this constitutes a type of WSI. Moreover, there are multiple ways to introduce the shear. For example, in Ref. [102], the shear was introduced with a glass slab placed on a rotating stage, such as in Fig. 18(a). By rotating the glass slab, the counter-propagating beams are laterally displaced in opposite directions, and the resulting interference pattern can be recorded for any shear.

The only downside of this technique is that the glass slab causes dispersion, which may separate the different frequency components such that the visibility of interference fringes is degraded when measuring large-bandwidth sources. Another possibility is to simply tilt one (or both) of the mirrors, as indicated in Fig. 18(b). However, the tilt will introduce a spatially varying path length difference, which may be a problem with sources featuring a large bandwidth.

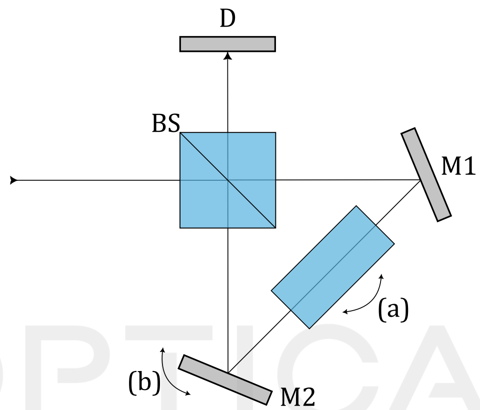

Fig. 18. Sagnac interferometer, where a beam is split into two by a beam splitter BS, and the copies are directed on a common path via mirrors M1 and M2. Shear is introduced with either (a) a rotating glass slab, or (b) by tilting one (or both) of the mirrors.

The field that arrives at the detector in a Sagnac-type interferometer is of the form

$$E(X;\omega) = \frac{1}{2}\left\{E_0(x;\omega) + E_0(x-s;\omega)\exp\left[i\Delta\phi(\omega)\right]\right\}, \quad \textbf{(82)}$$

where the shear s depends on the orientation of the mirrors and/or the tilt of the glass slab. In either case, the functional form of the field at the detector is of the same form as in a WSI, and thus these devices measure the same interference pattern.

F. Grating interferometers

In principle, one could produce an interferometer which measures spatial coherence with just a single grating. That is, if one can employ a grating with a sinusoidal profile, which will split the beam into two copies that are automatically sheared since they propagate towards different directions. However, a grating with a sinusoidal profile is difficult to fabricate and even small errors in the profile or possible impurities will cause light to diffract and/or scatter, hindering the operation of such a system. Therefore, it is often simpler to make a setup with a binary grating, block the undesired orders, and guide the remaining ones to the detection plane.

Such a setup was first considered in Ref. [104], where a $4f$ imaging system was used to guide the diffraction orders, and a suitable aperture was inserted at the Fourier plane in $2f$ as depicted in Fig. 19(a). In the original setup, the orders 0 and 1 were then guided to the detection plane. This had the disadvantage that the two orders propagated on different paths, and thus spatial and temporal coherence were mixed. In Ref. [105], the setup was further refined by allowing symmetric orders (± 1) through the setup and introducing shear with an SLM as shown in Fig. 19(b). A further simplification to the grating interferometer can be made by employing two binary gratings, G1 and G2, where the first splits and the second recombines the beams [106]. Since the gratings are binary, the zeroth order has a non-vanishing amplitude, but it is blocked at the back surface of G2. The shear can be introduced by shifting the gratings in tandem. One could instead shift the detector to achieve a similar shear, but this would change the distance to the observation plane and possibly alter the observed coherence function due to the extra propagation length. Additionally, from a mechanical perspective, it is simpler to move the gratings since it does not affect the alignment or introduce unwanted vibrations at the detector.

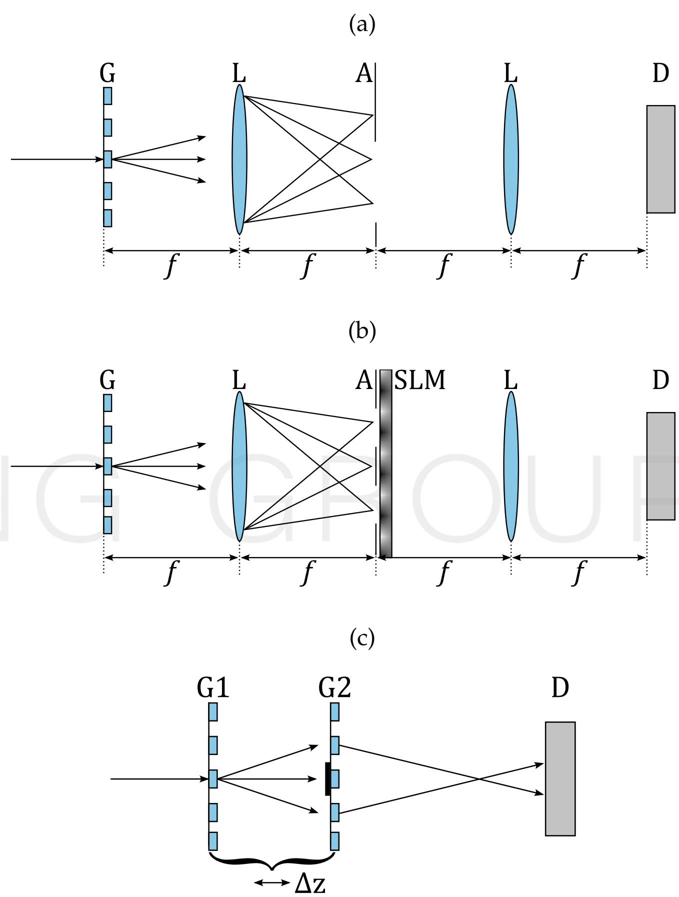

Fig. 19. Possible implementations of the grating interferometer. (a) Grating G and a $4f$ imaging system with lenses L, aperture A and detector D. The aperture allows only two diffraction orders (here 0 and 1). (b) A similar system, where orders ± 1 are allowed through, and the shear is accomplished with an SLM. (c) A double grating geometry, where the beam block is on the surface of the second grating G2. Here, the shear is introduced by translating the gratings together.

The grating interferometers form a large family of techniques, which have been used for spatial coherence measurements of exotic sources [107], as well as for other tasks. Their flexibility is attractive, although they require some micro- or nanofabrication. For example, the double grating interferometer in Fig. 19(c) is exceedingly simple, and it is able to correct small misalignments due to the employed geometry. Moreover, the beams arrive at the detection plane with practically zero path-length difference at all shears. But it too has a downside; different wavelength components produce differently scaled interference patterns (since the propagation angle depends on the wavelength). Hence, for broadband light, an imaging spectrometer needs to be used as a detector.

G. Obstacles

As a last example we consider the use of obstacles for measuring spatial correlations [108–111]. Out of all of the methods considered here, it is the only one that does not rely on interferometry. The method is intriguingly simple: first, one measures the intensity distribution of the beam, I_0, in the far-zone. Then, an obstacle is inserted at the source plane, and the new far-zone intensity distribution I_m is recorded. Note that the obstacle must be chosen such that the light remains paraxial. By investigating the difference between the two intensities, $\delta I = I_m - I_0$, it is possible to estimate the coherence at the source plane as in

$$W_1(\mathbf{r}_0, \Delta\mathbf{r}) \approx \frac{1}{\Lambda(\mathbf{r}_0, \Delta\mathbf{r})} \iint \delta I(\mathbf{r}_0, \mathbf{r}') \exp(ik\Delta\mathbf{r} \cdot \mathbf{r}')\mathrm{d}^2\mathbf{r}'. \quad \textbf{(83)}$$

Here $W_1(\mathbf{r}_0, \Delta\mathbf{r})$ is the leading term in a Taylor series expansion of $W_0(\mathbf{r}, \Delta\mathbf{r})$ around the centroid of the obstacle $\mathbf{r}_0$, and $\Lambda(\mathbf{r}_0, \Delta\mathbf{r})$ is the autocorrelation of the obstacle, whereas the primed coordinates denote far-zone quantities. As is evident, this method produces an approximation of the coherence function. Even if only the leading term is employed, the error only goes up to 12 % for completely coherent fields, and decreases relatively fast for lower coherence [109].

The obstacle can either be a phase discontinuity, or an amplitude object that produces a shadow. The shadow method is preferable, since the phase discontinuity method cannot measure small values of $\Delta\mathbf{r}$ reliably. Moreover, the measurement error is smallest for a field obeying the Schell-model and more general fields are difficult to estimate with this method. It is possible – at least in principle – to include higher order terms from the Taylor series to reduce the error, but this is rather cumbersome.

7. DISCUSSION

To limit the scope of the paper we made some assumptions at the start: restricting the discussion to second-order classical coherence and concentrating on paraxial (or beamlike) fields. However, as we saw in Sect. 3A, many of the sources we need to characterize produce non-paraxial radiation. Fortunately, the paraxial-domain techniques described above can be readily adapted to measure coherence of non-paraxial fields. Figure 20 illustrates some options for doing this.

In Fig. 20(a) we present a goniometric setup that can be used for coherence measurements in the far-field. Here the source is fixed, radiating into the positive half-space. In the far-zone the field becomes a diverging spherical wave with a linearly increasing radius of curvature R, which is independent of ω, and we are interested in measuring coherence at planes tangential to this reference sphere around a given (but arbitrary) central direction θ. This is accomplished by mounting the measurement setup D on a rotating arm of length R, moving along G over an interval $-\pi/2 < \theta < \pi/2$. Here D can be either a single-point detector (for intensity measurements), a spectrometer, or any instrument discussed above, with its input plane tangential to G. Alternatively, we may rotate the source itself to achieve the same goal, as illustrated in Fig. 20(b). The geometry (b) is more convenient particularly if the source is compact, such as a white

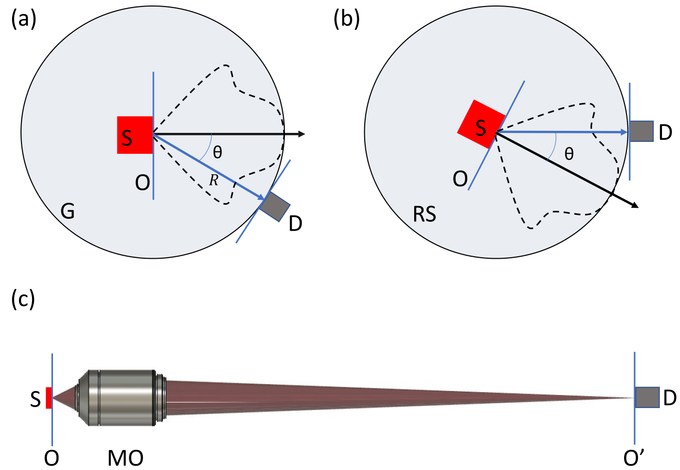

Fig. 20. Coherence measurements of non-paraxial fields. (a) Goniometric measurement with the instrument mounted on a rotation arm. (b) Goniometric measurement by rotating the source and keeping the measurement instrument at a fixed position. (c) Measurement of source-plane coherence using a secondary source generated by a high-NA imaging system with sufficient magnification. S: source at object plane O, D: detector, G: Goniometric sphere of radius R, RS: rotating stage, MO: microscope objective, O′: image plane of O.

LED, and it eliminates the need to rotate the entire measurement system.

The goniometric systems just discussed are particularly attractive if the source generating the strongly diverging field is quasihomogeneous. This is the case, for instance, if the source is an LED or a thermal one, limited in size by a (hard or apodizing) aperture with dimensions substantially larger than the coherence area in the source plane. In such circumstances the coherence area in the far-field is also small compared with the divergence of the field, as discussed qualitatively in Sect. 3A and more quantitatively in Sect. 4D. Hence, the assumption that far-field coherence can be measured by considering directions close to θ is well justified. Moreover, for quasihomogeneous fields only far-field intensity measurements are needed to determine the source-plane coherence and only far-field coherence measurements are needed to determine the source-plane intensity (Sect. 5.3.2 of [2], [112]), whereas in general the full CSD in the far-field needs to be measured to get the full source-plane CSD (Sect. 5.3.1 of [2]).

In the quasihomogeneous case the measurement of the low-frequency (LF, or non-evanescent) part of the far-field spectral density allows the use of inverse diffraction techniques to determine the complex degree of spectral coherence (see Sect. 5.3.3 of [2] and the references cited therein). It turns out that the source-plane coherence area has wavelength-scale dimensions, but can depend significantly on frequency. This effectively forbids direct source-plane coherence measurements, but it is possible to use imaging systems with a high numerical aperture (NA) and a large magnification to generate a secondary source at O′ that radiates paraxially as illustrated in Fig. 20(c). If the NA is sufficiently high to collect the entire diverging field, the spatial distribution of the spectral DOC across he secondary source is essentially a magnified version of that at the plane of the primary source. Thus, it can be measured if the magnification is sufficiently high to match the spatial resolution of the array detector. If, however, the radiation is highly divergent (extending up to $\theta \sim 90°$), as in the case of incoherent or Lambertian sources, the entire low-frequency part cannot be collected in practice. As a consequence, the DOC at the secondary source plane is not equal to that at the primary source (see Ref. [42] for a quantitative discussion).

We also restricted the discussion to stationary fields even though many of the sources discussed in Sect. 3A are nonstationary, with fields consisting of trains of pulses with durations depending strongly on the type of source. In this case, individual pulses may be considered as (deterministic) field realizations, over which ensemble averages can be taken to obtain either the two-frequency CSD – $W(\mathbf{r}_1, \mathbf{r}_2; \omega_1, \omega_2)$ – or the two-time MCF – $\Gamma(\mathbf{r}_1, \mathbf{r}_2; t_1, t_2)$. In view of Eq. (19), the correlation functions in the space-time and space-frequency domain are related via

$$\Gamma(\mathbf{r}_1, \mathbf{r}_2; t_1, t_2) = \iint_0^\infty W(\mathbf{r}_1, \mathbf{r}_2; \omega_1, \omega_2) \times \exp\left[i\left(\omega_1 t_1 - \omega_2 t_2\right)\right] \mathrm{d}\omega_1 \mathrm{d}\omega_2. \quad \mathbf{(84)}$$

Direct measurements of full correlation functions for nonstationary fields is notoriously difficult; the only straightforward way that we are aware of is to measure an ensemble of individual realization using nonlinear techniques for characterization of ultrashort pulses [113, 114] and then carry out the construction of the ensemble averages numerically.

However, if the measurements are done with 'slow' square-law detectors using devices discussed in Sect. 5, we obtain the time-averaged MCF, which depends only on the time difference:

$$\bar{\Gamma}(\mathbf{r}_1, \mathbf{r}_2; \Delta t) = \int_{-\infty}^{\infty} \Gamma(\mathbf{r}_1, \mathbf{r}_2; t, \Delta t) \mathrm{d}t = 2\pi \int_0^\infty W(\mathbf{r}_1, \mathbf{r}_2; \omega, \omega) \exp\left(-i\omega\Delta t\right) \mathrm{d}\omega, \quad \mathbf{(85)}$$

where the latter form follows from Eq. (84). Then, setting $\Delta t = 0$, the relation between easily measurable spatial coherence functions in the space-time and space-frequency domains becomes analogous to the corresponding relation for stationary fields.

Apart from the general scope limitations, there are many specific topics that are of current interest but could not be discussed here in detail. In some cases, custom-designed coherence measurement techniques have been developed for field characterization. One notable example is a recently introduced formalism that allows a unified analysis of coherence and orbital angular momentum of light fields [115]. The results were verified experimentally in Ref. [116] by employing a variant of Young's interferometer with two thin concentric annular apertures instead of pinholes.

8. CONCLUSIONS

We have described and compared the most important techniques for measuring the spatial coherence of light fields in a way that is hoped to be accessible to both experimentally and theoretically oriented readers. The mathematical formulation of partially coherent light in the space-frequency and space-time domains was presented in sufficient detail to understand the operating principles and fundamental limitations of the methods covered. Instrumentation issues were addressed in some detail, as well as practical aspects related to data acquisition speed and the light power levels required for reliable measurements.

To conclude, techniques based on wavefront folding and shearing interferometers (WFIs and WSIs) generally outperform all other methods. The light efficiency is such that if one can measure the spatial intensity (spectral density) of the incident field, one can also measure the complex degree of spatial coherence in the space-time (space-frequency) domain. Both WFI and WSI systems can be implemented in either 1D or 2D form. The performance of the two is essentially identical, but it is worth noting that WSIs measure the correlations directly between two cartesian points $\mathbf{r}_1$ and $\mathbf{r}_2$, while WFIs give the results more naturally in average and difference coordinates $\bar{\mathbf{r}} = (\mathbf{r}_1 + \mathbf{r}_2)/2$ and $\Delta\mathbf{r} = \mathbf{r}_2 - \mathbf{r}_1$. In 1D folding/shearing implementations, spectral information can be measured simultaneously with spatial information along one spatial dimension by adding a spectrometer in the instrument. The 2D implementations allow the measurement of full 4D correlation functions (also in practise), but only for a single spectral band at a time.

Acknowledgments. This work was partially funded by the Academy of Finland (320165,320166,349396). We acknowledge the substantial contributions of Henri Partanen and Kimmo Saastamoinen to the development of in-house implementations of several coherence measurements techniques covered in this review.

Disclosures. The authors declare no conflicts of interest.

Data availability. Data underlying the results presented in this paper are not publicly available at this time but may be obtained from the authors upon reasonable request.

REFERENCES

1. M. Born and E. Wolf, *Principles of Optics: Electromagnetic Theory of Propagation, Interference and Diffraction of Light* (Cambridge University Press, 1999), 7th ed.
2. L. Mandel and E. Wolf, *Optical Coherence and Quantum Optics* (Cambridge University Press, 1995).
3. E. Wolf, "Invariance of the spectrum of light on propagation," Phys. Rev. Lett. **56**, 1370–1372 (1986).
4. E. Wolf, "Unified theory of coherence and polarization of random electromagnetic beams," Phys. Lett. A **312**, 263–267 (2003).
5. G. Gbur and T. D. Visser, "Young's interference experiment: Past, present, and future," Prog. Opt. **67**, 275–343 (2022).
6. I. Newton, *Opticks: or, A treatise of the reflexions, refractions, inflexions and colours of light.* (London: Printed for Sam. Smith, and Benj. Walford., 1704).
7. R. Descartes, *Le Monde* (Paris: M. Bobin et N. le Gras, 1664).
8. T. Young, "II. the Bakerian Lecture. on the theory of light and colours," Philos. Trans. Royal Soc. **92**, 12–48 (1802).
9. T. Young, "I. the Bakerian Lecture. experiments and calculations relative to physical optics," Philos. Trans. Royal Soc. **94**, 1–16 (1804).
10. T. Young, *A course of lectures on natural philosophy and the mechanical arts* (London: printed for Joseph Johnson, St. Paul's Church Yard, 1807).
11. E. Verdet, "Étude sur la constitution de la lumière non polarisée et de la lumière partiellement polarisée," Ann. Sci. Éc. Norm. Supér. **2**, 291–316 (1865).
12. M. von Laue, "Die Entropie von partiell kohärenten Strahlenbündeln," Ann. Phys. **328**, 1–43 (1907).
13. P. H. van Cittert, "Die wahrscheinliche Schwingungsverteilung in einer von einer Lichtquelle direkt oder mittels einer Linse beleuchteten Ebene," Physica **1**, 201–210 (1934).
14. F. Zernike, "The concept of degree of coherence and its application to optical problems," Physica **5**, 785–795 (1938).
15. M. Born, *Optik* (Springer Berlin, 1933).
16. M. Bertolotti, *The History of the Laser* (CRC Press, 2004), 1st ed.
17. A. L. Schawlow and C. H. Townes, "Infrared and optical masers," Phys. Rev. **112**, 1940–1949 (1958).
18. E. Wolf, "A macroscopic theory of interference and diffraction of light from finite sources," Nature **172**, 535–535 (1953).

19. E. Wolf, “Partially coherent optical fields,” Vistas Astron. **1**, 385–394 (1955).
20. E. Wolf, “Intensity fluctuations in stationary optical fields,” Phil. Mag. **15**, 351–354 (1957).
21. E. Wolf, “A macroscopic theory of interference and diffraction of light from finite sources II. Fields with a spectral range of arbitrary width,” Proc. R. Soc. London, Ser. A **230**, 246–265 (1955).
22. E. Wolf and E. Collett, “Partially coherent sources which produce the same far-field intensity distribution as a laser,” Opt. Commun. **25**, 293–296 (1978).
23. E. Collett and E. Wolf, “Is complete spatial coherence necessary for the generation of highly directional light beams?” Opt. Lett. **2**, 27–29 (1978).
24. E. Collett and E. Wolf, “New equivalence theorems for planar sources that generate the same distributions of radiant intensity,” J. Opt. Soc. Am. **69**, 942–950 (1979).
25. P. De Santis, F. Gori, G. Guattari, and C. Palma, “An example of a Collett–Wolf source,” Opt. Commun. **29**, 256–260 (1979).
26. F. Gori, “Collett–Wolf sources and multimode lasers,” Opt. Commun. **34**, 301–305 (1980).
27. F. Gori, “Directionality and spatial coherence,” Opt. Acta **27**, 1025–1034 (1980).
28. F. Gori and C. Palma, “Partially coherent sources which give rise to highly directional light beams,” Opt. Commun. **27**, 185–188 (1978).
29. G. M. Morris and D. Faklis, “Effects of source correlation on the spectrum of light,” Opt. Commun. **62**, 5–11 (1987).
30. D. Faklis and G. M. Morris, “Spectral shifts produced by source correlations,” Opt. Lett. **13**, 4–6 (1988).
31. F. Gori, “Matrix treatment for partially polarized, partially coherent beams,” Opt. Lett. **23**, 241–243 (1998).
32. F. Gori, M. Santarsiero, S. Vicalvi, R. Borghi, and G. Guattari, “Beam coherence-polarization matrix,” Pure Appl. Opt. J. Eur. Opt. Soc. Part A **7**, 941–951 (1998).
33. N. Stelmakh and M. Flowers, “Measurement of spatial modes of broad-area diode lasers with 1-GHz resolution grating spectrometer,” IEEE Photon. Technol. Lett. **18**, 1618–1620 (2006).
34. H. Partanen, J. Tervo, and J. Turunen, “Spatial coherence of broad-area laser diodes,” Appl. Opt. **52**, 3221–3228 (2013).
35. E. Saldin, E. V. Schneidmiller, and M. V. Yurkov, *The Physics of Free Electron Lasers* (Springer, 2000).
36. A. Singer, I. A. Vartanyants, M. Kuhlmann, S. Duesterer, R. Treusch, and J. Feldhaus, “Transverse-coherence properties of the free-electron-laser FLASH at DESY,” Phys. Rev. Lett. **101**, 254801 (2008).
37. I. A. Vartanyants, A. Singer, A. P. Mancuso, O. M. Yefanov, A. Sakdinawat, Y. Liu, E. Bang, G. J. Williams, G. Cadenazzi, B. Abbey, H. Sinn, D. Attwood, K. A. Nugent, E. Weckert, T. Wang, D. Zhu, B. Wu, C. Graves, A. Scherz, J. J. Turner, W. F. Schlotter, M. Messerschmidt, J. Lüning, Y. Acremann, P. Heimann, D. C. Mancini, V. Joshi, J. Krzywinski, R. Soufli, M. Fernandez-Perea, S. Hau-Riege, A. G. Peele, Y. Feng, O. Krupin, S. Moeller, and W. Wurth, “Coherence properties of individual femtosecond pulses of an x-ray free-electron laser,” Phys. Rev. Lett. **107**, 144801 (2011).
38. A. Singer, F. Sorgenfrei, A. P. Mancuso, N. Gerasimova, O. M. Yefanov, J. Gulden, T. Gorniak, T. Senkbeil, A. Sakdinawat, Y. Liu, D. Attwood, S. Dziarzhytski, D. D. Mai, R. Treusch, E. Weckert, T. Salditt, A. Rosenhahn, W. Wurth, and I. A. Vartanyants, “Spatial and temporal coherence properties of single free-electron laser pulses,” Opt. Express **20**, 17480–17495 (2012).
39. A. Verhoeven, C. Hellmann, F. Wyrowski, M. Idir, and J. Turunen, “Genuine-field modeling of partially coherent X-ray imaging systems,” J. Synchrotron Radiat. **27**, 1307–1319 (2020).
40. J. Cho, J. H. Park, J. K. Kim, and E. F. Schubert, “White light-emitting diodes: History, progress, and future,” Laser Photonics Rev. **11**, 1600147 (2017).
41. C. Weissbuch, “Review—on the search for efficient solid state light emitters: Past, present, future,” ECS J. Solid State Sci. Eng. **9**, 016022 (2020).
42. A. Halder and J. Turunen, “Spectral coherence of white leds,” Photon. Res. **10**, 2460–2470 (2022).
43. R. R. Alfano and S. L. Shapiro, “Emission in the region 4000 to 7000 Å via four-photon coupling in glass,” Phys. Rev. Lett. **24**, 584–587 (1970).
44. R. R. Alfano and S. L. Shapiro, “Observation of self-phase modulation and small-scale filaments in crystals and glasses,” Phys. Rev. Lett. **24**, 592–594 (1970).
45. F. Silva, D. R. Austin, A. Thai, M. Baudisch, M. Hemmer, D. Faccio, A. Couairon, and J. Biegert, “Multi-octave supercontinuum generation from mid-infrared filamentation in a bulk crystal,” Nat. Commun. **3**, 807 (2012).
46. J. M. Dudley, G. Genty, and S. Coen, “Supercontinuum generation in photonic crystal fiber,” Rev. Mod. Phys. **78**, 1135–1184 (2006).
47. J. E. Beetar, M. Nrisimhamurty, T.-C. Truong, G. C. Nagar, Y. Liu, J. Nesper, O. Suarez, F. Rivas, Y. Wu, B. Shim, and M. Chini, “Multioctave supercontinuum generation and frequency conversion based on rotational nonlinearity,” Sci. Adv. **6**, eabb5375 (2020).
48. A. Halder, V. Jukna, M. Koivurova, A. Dubietis, and J. Turunen, “Coherence of bulk-generated supercontinuum,” Photon. Res. **7**, 1345–1353 (2019).
49. G. Genty, A. T. Friberg, and J. Turunen, “Chapter two - coherence of supercontinuum light,” in *Progress in Optics,* vol. 61 T. D. Visser, ed. (Elsevier, 2016), pp. 71–112.
50. J. W. Goodman, *Introduction to Fourier optics* (Roberts and Company Publishers, 2005), 2nd ed.
51. A. Schell, “A technique for the determination of the radiation pattern of a partially coherent aperture,” IEEE Trans. Antennas Propag. **15**, 187–188 (1967).
52. E. Tervonen, J. Turunen, and A. T. Friberg, “Transverse laser-mode structure determination from spatial coherence measurements: experimental results,” Appl. Phys. B **49**, 409–414 (1989).
53. W. T. Welford, *Aberrations of Optical Systems* (Adam Hilger, 1986).
54. J. Ellis and A. Dogariu, “Complex degree of mutual polarization,” Opt. Lett. **29**, 536–538 (2004).
55. O. Korotkova and E. Wolf, “Generalized Stokes parameters of random electromagnetic beams,” Opt. Lett. **30**, 198–200 (2005).
56. J. Tervo, T. Setälä, A. Roueff, P. Réfrégier, and A. T. Friberg, “Two-point Stokes parameters: interpretation and properties,” Opt. Lett. **34**, 3074–3076 (2009).
57. O. Korotkova, *Random Light Beams: Theory and Applications* (CRC Press, 2014).
58. J. Tervo, T. Setälä, and A. T. Friberg, “Degree of coherence for electromagnetic fields,” Opt. Express **11**, 1137–1143 (2003).
59. A. T. Friberg and T. Setälä, “Electromagnetic theory of optical coherence [invited],” J. Opt. Soc. Am. A **33**, 2431–2442 (2016).
60. J. T. Foley and M. Zubairy, “The directionality of Gaussian Schell-model beams,” Opt. Commun. **26**, 297–300 (1978).
61. P. D. Santis, F. Gori, G. Guattari, and C. Palma, “Anisotropic Gaussian Schell-model sources,” Opt. Acta: Int. J. Opt. **33**, 315–326 (1986).
62. J. Farina, L. Narducci, and E. Collett, “Generation of highly directional beams from a globally incoherent source,” Opt. Commun. **32**, 203–208 (1980).
63. Q. He, J. Turunen, and A. T. Friberg, “Propagation and imaging experiments with Gaussian Schell-model beams,” Opt. Commun. **67**, 245–250 (1988).
64. A. T. Friberg and R. J. Sudol, “Propagation parameters of Gaussian Schell-model beams,” Opt. Commun. **41**, 383–387 (1982).
65. R. Simon, E. C. G. Sudarshan, and N. Mukunda, “Generalized rays in first-order optics: Transformation properties of Gaussian Schell-model fields,” Phys. Rev. A **29**, 3273–3279 (1984).
66. J. Turunen and A. Friberg, “Matrix representation of Gaussian Schell-model beams in optical systems,” Opt. & Laser Technol. **18**, 259–267 (1986).
67. A. T. Friberg and J. Turunen, “Imaging of Gaussian Schell-model sources,” J. Opt. Soc. Am. A **5**, 713–720 (1988).
68. Y. Li and E. Wolf, “Radiation from anisotropic Gaussian Schell-model sources,” Opt. Lett. **7**, 256–258 (1982).
69. F. Gori, “Mode propagation of the field generated by Collett–Wolf Schell-model sources,” Opt. Commun. **46**, 149–154 (1983).

70. P. W. Milonni and J. H. Eberly, *Lasers* (Wiley, 1988).
71. A. Starikov and E. Wolf, "Coherent-mode representation of Gaussian Schell-model sources and of their radiation fields," J. Opt. Soc. Am. **72**, 923–928 (1982).
72. M. Koivurova, C. Ding, J. Turunen, and L. Pan, "Partially coherent isodiffracting pulsed beams," Phys. Rev. A **97**, 023825 (2018).
73. F. Gori and R. Grella, "Shape invariant propagation of polychromatic fields," Opt. Commun. **49**, 173–177 (1984).
74. H. Karttunen, P. Kröger, H. Oja, M. Poutanen, and K. J. Donner, *Fundamental Astronomy* (Springer Berlin, 2017).
75. R. H. Katyl, "Compensating optical systems. part 3: achromatic Fourier transformation," Appl. Opt. **11**, 1255–1260 (1972).
76. G. M. Morris, "Diffraction theory for an achromatic Fourier transformation," Appl. Opt. **20**, 2017–2025 (1981).
77. G. M. Morris, "An ideal achromatic Fourier processor," Opt. Commun. **39**, 143–147 (1981).
78. E. Tajahuerce, V. Climent, J. Lancis, M. Fernández-Alonso, and P. Andrés, "Achromatic Fourier transforming properties of a separated diffractive lens doublet: theory and experiment," Appl. Opt. **37**, 6164–6173 (1998).
79. K. Saastamoinen, J. Tervo, J. Turunen, P. Vahimaa, and A. T. Friberg, "Spatial coherence measurement of polychromatic light with modified Young's interferometer," Opt. Express **21**, 4061–4071 (2013).
80. H. Partanen, J. Turunen, and J. Tervo, "Coherence measurement with digital micromirror device," Opt. Lett. **39**, 1034–1037 (2014).
81. H. Partanen, A. T. Friberg, T. Setälä, and J. Turunen, "Spectral measurement of coherence Stokes parameters of random broadband light beams," Photon. Res. **7**, 669–677 (2019).
82. H. W. Wessely and J. O. Bolstad, "Interferometric technique for measuring the spatial-correlation function of optical radiation fields," J. Opt. Soc. Am. **60**, 678–682 (1970).
83. J. B. Breckinridge, "Coherence interferometer and astronomical applications," Appl. Opt. **11**, 2996–2998 (1972).
84. H. Arimoto and Y. Ohtsuka, "Measurements of the complex degree of spectral coherence by use of a wave-front-folded interferometer," Opt. Lett. **22**, 958–960 (1997).
85. D. Malacara, *Optical Shop Testing* (Wiley, 1992).
86. A. Efimov, "Lateral-shearing, delay-dithering Mach–Zehnder interferometer for spatial coherence measurement," Opt. Lett. **38**, 4522–4525 (2013).
87. A. Efimov, "Spatial coherence at the output of multimode optical fibers," Opt. Express **22**, 15577–15588 (2014).
88. M. Koivurova, H. Partanen, J. Lahyani, N. Cariou, and J. Turunen, "Scanning wavefront folding interferometers," Opt. Express **27**, 7738–7750 (2019).
89. A. Halder, H. Partanen, A. Leinonen, M. Koivurova, T. K. Hakala, T. Setälä, J. Turunen, and A. T. Friberg, "Mirror-based scanning wavefront-folding interferometer for coherence measurements," Opt. Lett. **45**, 4260–4263 (2020).
90. F. Gori, G. Guattari, C. Palma, and C. Padovani, "Specular cross-spectral density functions," Opt. Commun. **68**, 239–243 (1988).
91. H. Partanen, N. Sharmin, J. Tervo, and J. Turunen, "Specular and antispecular light beams," Opt. Express **23**, 28718–28727 (2015).
92. D. Das, A. Halder, H. Partanen, M. Koivurova, and J. Turunen, "Propagation of Bessel-correlated specular and antispecular beams," Opt. Express **30**, 5709–5721 (2022).
93. B. O. Asamoah, H. Partanen, S. Mohamed, J. Heikkinen, A. Halder, M. Koivurova, M. Nečada, T. Setälä, J. Turunen, A. T. Friberg, and T. K. Hakala, "Polarization dependent beaming properties of a plasmonic lattice laser," New J. Phys. **23**, 063037 (2021).
94. M. Santarsiero and R. Borghi, "Measuring spatial coherence by using a reversed-wavefront Young interferometer," Opt. Lett. **31**, 861–863 (2006).
95. Y. Mejía and A. I. González, "Measuring spatial coherence by using a mask with multiple apertures," Opt. Commun. **273**, 428–434 (2007).
96. A. I. González and Y. Mejía, "Nonredundant array of apertures to measure the spatial coherence in two dimensions with only one interferogram," J. Opt. Soc. Am. A **28**, 1107–1113 (2011).
97. J. Duarte, A. I. Gonzalez, R. Cassin, R. Nicolas, M. Kholodstova, W. Boutu, M. Fajardo, and H. Merdji, "Single-shot spatial coherence characterization of x-ray ultrafast sources," Opt. Lett. **46**, 1764–1767 (2021).
98. S. Divitt, Z. J. Lapin, and L. Novotny, "Measuring coherence functions using non-parallel double slits," Opt. Express **22**, 8277–8290 (2014).
99. K. Saastamoinen, L.-P. Leppänen, I. Vartiainen, A. T. Friberg, and T. Setälä, "Spatial coherence of light measured by nanoscattering," Optica **5**, 67–70 (2018).
100. L.-P. Leppänen, K. Saastamoinen, A. T. Friberg, and T. Setälä, "Detection of electromagnetic degree of coherence with nanoscatterers: comparison with Young's interferometer," Opt. Lett. **40**, 2898–2901 (2015).
101. K. Saastamoinen, H. Partanen, A. T. Friberg, and T. Setälä, "Probing the electromagnetic degree of coherence of light beams with nanoscatterers," ACS Photonics **7**, 1030–1035 (2020).
102. C. Iaconis and I. A. Walmsley, "Direct measurement of the two-point field correlation function," Opt. Lett. **21**, 1783–1785 (1996).
103. R. R. Naraghi, H. Gemar, M. Batarseh, A. Beckus, G. Atia, S. Sukhov, and A. Dogariu, "Wide-field interferometric measurement of a nonstationary complex coherence function," Opt. Lett. **42**, 4929–4932 (2017).
104. W. H. Carter, "Measurement of second-order coherence in a light beam using a microscope and a grating," Appl. Opt. **16**, 558–563 (1977).
105. L. Pan, X. Chao, Z.-C. Ren, H.-T. Wang, and J. Ding, "Measuring spatial coherence by using a lateral shearing interferometry," Appl. Opt. **58**, 56–61 (2019).
106. M. Koivurova, H. Partanen, J. Turunen, and A. T. Friberg, "Grating interferometer for light-efficient spatial coherence measurement of arbitrary sources," Appl. Opt. **56**, 5216–5227 (2017).
107. F. Pfeiffer, O. Bunk, C. Schulze-Briese, A. Diaz, T. Weitkamp, C. David, J. F. van der Veen, I. Vartanyants, and I. K. Robinson, "Shearing interferometer for quantifying the coherence of hard x-ray beams," Phys. Rev. Lett. **94**, 164801 (2005).
108. J. J. A. Lin, D. Paterson, A. G. Peele, P. J. McMahon, C. T. Chantler, K. A. Nugent, B. Lai, N. Moldovan, Z. Cai, D. C. Mancini, and I. McNulty, "Measurement of the spatial coherence function of undulator radiation using a phase mask," Phys. Rev. Lett. **90**, 074801 (2003).
109. S. Cho, M. A. Alonso, and T. G. Brown, "Measurement of spatial coherence through diffraction from a transparent mask with a phase discontinuity," Opt. Lett. **37**, 2724–2726 (2012).
110. J. K. Wood, K. A. Sharma, S. Cho, T. G. Brown, and M. A. Alonso, "Using shadows to measure spatial coherence," Opt. Lett. **39**, 4927–4930 (2014).
111. H. Hooshmand-Ziafi, M. Dashtdar, and K. Hassani, "Measurement of the full complex degree of coherence using Fresnel diffraction from a phase discontinuity," Opt. Lett. **45**, 3737–3740 (2020).
112. W. H. Carter and E. Wolf, "Coherence and radiometry with quasihomogeneous planar sources∗," J. Opt. Soc. Am. **67**, 785–796 (1977).
113. I. A. Walmsley and C. Dorrer, "Characterization of ultrashort electromagnetic pulses," Adv. Opt. Photon. **1**, 308–437 (2009).
114. R. Trebino, *Frequency-Resolved Optical Gating: The Measurement of Ultrashort Laser Pulses* (Kluwer Academic Publishers, 2000).
115. O. Korotkova and G. Gbur, "Unified matrix representation for spin and orbital angular momentum in partially coherent beams," Phys. Rev. A **103**, 023529 (2021).
116. Z. Yang, H. Wang, Y. Chen, F. Wang, G. Gbur, O. Korotkova, and Y. Cai, "Measurement of the coherence-orbital angular momentum matrix of a partially coherent beam," Opt. Lett. **47**, 4467–4470 (2022).